ADVANCED SUSTAINABLE SYSTEMS
www.advsustainsys.com

Dual Charge Transfer Mechanisms in Intimately Bonded S-scheme Heterojunction Photocatalyst with Expeditious Activity toward Environmental Remediation

Potlako J. Mafa, Mope E. Malefane, Francis Opoku, Adewale O. Oladipo, Gcina Mamba, Tunde L. Yusuf, Jemal Fito Nure, Sogolo L. Lebelo, Dan Liu, Jianzhou Gui, Bhekie B. Mamba, and Alex T. Kuvarega*

Fabrication of a photocatalyst with the desired characteristics of high charge isolation and expeditious photocatalytic performance is crucial in photocatalysis. Constructing an interfacial chemically bonded S-scheme heterojunction is an effective path to the realization of high interfacial charge transfer and performance. Herein, Mg-Bi_2O_3/dark gray g-C_3N_4 (MBOdCN) S-scheme heterojunction with Bi-N bond bridges is successfully constructed using an in situ calcination strategy for oxytetracycline (OTC) degradation. The MBOdCN (1:5) displays outstanding performance with efficiency and rate constant of 99.56% and 0.0235 min^{-1}, respectively. The synergy of n-π^* transition, Mg defects, and Bi–N bond bridges in the MBOdCN enhances the performance of the S-scheme heterojunction. X-ray photoelectron spectroscopy (XPS) analysis, work function measurements, and density functional theory (DFT) reveal the formation of MBOdCN S-scheme heterojunction. In this system, trapping experiments and electron-spin resonance (ESR) spectroscopy confirm the predominance of $^{\bullet}O_2^-$ > h^+ > $^{\bullet}OH$ during OTC degradation. The degradation pathways and byproducts are investigated with LC-MS and the toxicity study is undertaken on the OTC degradation byproducts and photocatalytic materials. This work provides a holistic understanding of the novel S-scheme heterojunction by introducing interfacial chemical bond bridges and defects as dual charge transfer channels.

1. Introduction

Antibiotics such as tetracyclines are essential for human and animal health; hence, their production and consumption have continued to increase. This increase in consumption has led to their frequent detection in the environment, including aquatic systems.[1] Generally, these pharmaceutical drugs enter the environment via several routes, including improper disposal of unused or expired medications, wastewater effluents, and animal manure.[2,3] Among the tetracyclines, oxytetracycline (OTC) which is widely used for the treatment of human and animal infections caused by both Gram-positive and Gram-negative bacteria, has been detected in aquatic environments at concentrations ranging from a few μg L^{-1} to hundreds of mg L^{-1}.[2,4] Owing to its environmental persistence and poor removal by conventional water treatment technologies, the presence of OTC in water poses a serious health risk to humanity and the entire ecological system. Undoubtedly, the

P. J. Mafa, M. E. Malefane, G. Mamba, D. Liu, J. Gui, B. B. Mamba, A. T. Kuvarega
Institute for Nanotechnology and Water Sustainability
College of Science
Engineering and Technology
University of South Africa
Florida Campus, Johannesburg 1709, South Africa
E-mail: mafapj@unisa.ac.za

The ORCID identification number(s) for the author(s) of this article can be found under https://doi.org/10.1002/adsu.202401070

DOI: 10.1002/adsu.202401070

F. Opoku
Department of Chemistry
Kwame Nkrumah University of Science and Technology
Kumasi 00233, Ghana

A. O. Oladipo, S. L. Lebelo
Department of Life and Consumer Sciences
College of Agriculture and Environmental Sciences
University of South Africa
Private Bag X06 Florida, Johannesburg 1709, South Africa

T. L. Yusuf
Department of Chemistry
Faculty of Natural and Agricultural Sciences
University of Pretoria
Hatfield, Pretoria 0028, South Africa

J. F. Nure
School of Chemical and Metallurgical Engineering
University of the Witwatersrand
1 Jorissen St, Johannesburg 2000, South Africa

presence of OTC poses an immediate threat to the environment and human health. With conventional water treatment processes rendered inadequate for removing antibiotics such as OTC, semiconductor photocatalysis has captured more scientific attention for removing antibiotics from water. This technique is known for its operation under ambient conditions, reusability of the catalyst, non-selectivity, and the possibility of exploiting solar light for catalyst activation.[5–8] Different photocatalytic heterojunctions such as type-I, type-II, type-III, and Z-scheme families have been developed and explored for various environmental remediation.[9–13] Although these photocatalytic mechanisms made a breakthrough in research, they are clouded by numerous thermodynamics, kinetics, and energy loss which are unfavorable for photocatalytic reactions.[14–16]

Recently, Yu and co-workers pioneered the concept of the Step-scheme (S-scheme) heterojunction, attracting massive scientific attention as the charge transfer and mechanism were well-articulated with high redox capabilities.[17] The S-scheme heterojunctions are composed of a minimum of two semiconductor photocatalysts, where one is an oxidative photocatalyst (OP) and the other is a reductive photocatalyst (RP).[18,19] The OP possesses greater work function accompanied by a lower Fermi level while the opposite applies in the RP.[20] The photocatalysts must have well-aligned staggered bands to enhance the built-in interfacial electric field (IEF) generation that propels the reduction of spatial charge carrier complexation and upward/downward band-bending for the creation of high redox potentials for reduction and oxidation reactions. Owing to its superiority and scientific rationality, the S-scheme mechanism of charge transfer has gained huge popularity.[21] The most crucial step in constructing highly efficient S-scheme photocatalytic heterojunctions entails a well-informed selection of appropriate RP and OP. Bismuth-based photocatalysts such as bismuth oxide (Bi_2O_3) have gained substantial recognition for S-scheme heterojunction formation. This material relies on the hybridization between the filled 6s orbitals of Bi and the O 2p orbitals of trivalent Bi (Bi^{3+}). Bi_2O_3 is known for its thermodynamic stability, non-toxic, low cost, and moderate optical properties, allowing it to utilize visible light (E_g = 2.0–3.9 eV).[22,23] However, recent studies revealed that the photocatalytic performance of Bi_2O_3 can be enhanced through the formation of S-scheme heterojunction due to its high oxidative power.[24–26] For example, Zhang et al.[27] successfully constructed Bi_2O_3@LHDs S-scheme heterojunction with Bi_2O_3 as the OP, to remarkably enhance the photocatalytic performance of the composite. The boosted performance was credited to the created built-in electric field (BIEF) and the formation of S-scheme heterojunction. Majhi et al.[28] used Bi_2O_3 as the OP for the construction of a highly efficient plasmonic $Bi_2O_3/CuBi_2O_4$ S-scheme heterojunction. On the other hand, our group reported on the formation of trimetal oxides/Bi_2O_3 S-scheme heterojunction that was confirmed through X-ray photoelectron spectroscopy (XPS) analysis and DFT calculations.[18] The formed S-type heterojunction displayed an expeditious charge transfer rate which could be linked to the built-in interfacial electrical field between the RP and OP in the system. Other S-scheme systems where Bi_2O_3 has been used involved three components or doping of one component with the primary aim of enhancing performance by lowering the rate of charge complexation.[24,26,29] It is always important to consider other photocatalytic materials when an S-scheme heterojunction is constructed using Bi_2O_3 as an OP. As such, it can be inferred that the construction of an S-scheme heterojunction photocatalyst using graphitic carbon nitride (g-C_3N_4) and Bi_2O_3 cannot only promote a high rate of charge detachment but also increase the RP and OP electrons and holes enrichment for the production of more radicals. Specifically, g-C_3N_4 boasts of a unique set of intrinsic properties such as the ease of fabrication, tunable structure, non-toxicity, metal-free nature, and high reduction potential, which collectively position it as an ideal component of S-scheme heterojunctions.[20,30,31]

Most recently, chemically bonded S-scheme heterojunctions, wherein the flow of charge is through the formed chemical bond between the RP and OP, have emerged as ideal interfacial configurations. This configuration is pursued since the conventional S-scheme heterojunction photocatalysts face a daunting challenge of weak interfacial contact and inherent low charge transfer efficiency.[32,33] Different chemically bonded heterojunctions including single or dual bonding such as Mg-N in MgO/g-C_3N_4,[34] Co-C in GDY/$CoTiO_3$,[35] Bi-O in $Bi_2Sn_2O_7$/BiOBr,[36] Co-S_x in 2D/2D CoAl-LDHs/$ZnIn_2S_4$,[37] Bi-N in $Bi_{12}O_{17}Br_2$/g-C_3N_4,[20] Bi-S in BiOBr/Bi_2S_3,[38] Se-P in In_2Se_3/Ag_3PO_4,[39] Mo-O in CeO_2/Mo-S,[40] N-Bi-O in Bi_2MoO_6/Bi-CN,[41] In-O-Mo in In_2O_3/Bi_2MoO_6,[42] In-O-Sn in $ZnIn_2S_4/SnS_2$,[43] In-O-Cd in In_2O_3/CdSe-DETA,[32] and Nd-O-C in 2D/2D Nb_2O_5/g-C_3N_4[44] have been explored for various photocatalytic applications involving S-scheme systems. In all the reports, the photoinduced charge carriers were effectively transported via the chemical bond bridges resulting in improved excitonic isolation and the production of more reactive species to take part in the photocatalytic process.[45] The chemical bonding occurs at the atomic level to enhance interfacial contact, thus Bi_2O_3 (OP) with its bismuth atom can easily coordinate with g-C_3N_4 (RP) with more electron-rich nitrogen atoms in its structure to construct a novel S-scheme heterojunction photocatalyst.[41,43,46] So far, there are no reports on the establishment of a chemically bonded S-scheme heterojunction photocatalyst between Mg-Bi_2O_3 (MBO) and a novel carbon-rich dark grey g-C_3N_4 (dCN) with boosted charge transfer emanating from Mg defects and Bi-N chemical bond.

In this study, a novel MBOdCN S-scheme heterojunction featuring well-defined Bi-N interfacial chemical linkages and Mg defects was prepared by an in situ calcination method. The supramolecule precursor of dark gray g-C_3N_4 made from tannic-cyanuric acid-melamine-cetyltrimethylammonium bromide (CTAB) was mixed with Mg-Bi_2O_3 and calcined to create a Bi-N chemical bond linking the two photocatalytic materials. The interfacial bonding bridges serve as efficient channels for photoexcitons transfer and improve the stability of the S-scheme heterojunction, thereby sustaining efficient photocatalytic performance. Various characterization techniques and photocatalytic degradation of OTC were executed to study the

D. Liu, J. Gui, B. B. Mamba
State Key Laboratory of Separation Membranes and Membrane Processes
Tianjin Key Laboratory of Green Chemical Technology and Process Engineering
School of Chemistry and Chemical Engineering
Tiangong University
Tianjin 300387, China

structural integrity of MBOdCN S-scheme photocatalyst versus the pristine catalysts (MBO and dCN). Additionally, DFT calculations were performed to get more insights into the optical and electronic properties of the materials. A toxicity study of the OTC degradation byproducts (DP) and photocatalytic materials was performed. This work holds promising prospects for the exploitation of chemically bonded S-scheme heterojunctions with boosted interfacial charge transfer and photocatalytic efficiency.

2. Results and Discussion

2.1. Structural and Morphological Characterizations

The physicochemical identities of the materials were analyzed using X-ray diffraction (XRD), Raman, and Fourier transform infrared (FTIR) spectroscopy, as illustrated in **Figure 1**. The XRD patterns of the pristine materials are shown in Figure 1a while those of the composites are depicted in Figure 1b. The patterns of MBO show the fingerprints of monoclinic α-Bi_2O_3, with the most intense peak located at 27.64° having a d-spacing of 0.32 nm and indexed to the (120) plane. The monoclinic lattice parameters are $a = 0.58496$ nm, $b = 0.81648$ nm, and $c = 0.75101$ nm, corresponding to the P21/c space group according to JCPDS No. 71–0465.[18] However, as much as the results display the XRD pattern of α-Bi_2O_3, there was a peak located at approximately 46.57° (d-spacing is 0.19 nm) corresponding to the (200) lattice plane and could be indexed to the cubic MgO periclase with the following cell parameters: $a = b = c = 0.38971$ nm and the Fm-3m(225) space group according to JCPDS No. 85–5643. This indicates the presence of Mg in the crystal structure of α-Bi_2O_3. As shown in Figure 1a, the XRD pattern of dCN displays a typical diffractogram of the graphitic carbon nitride phase bearing distinct peaks at approximately 2θ of 13.05° and 27.32° with d-spacings of 0.69 and 0.32 nm, respectively. These peaks correspond to the (100) and (002) crystalline planes of the hexagonal g-C_3N_4 phase according to JCPDS No. 87–1526,[47] and they emanate from the more interplane structural packing of tri-s-triazine and interlayer structural stacking of aromatic systems.[48] Owing to the increased amount of carbon in dCN, its XRD pattern appears amorphous. Figure 1b depicts the XRD patterns of the composite materials and, it can be seen that at a 3:1 ratio, α-Bi_2O_3 maintained its crystallinity while there was a remarkable change in crystallinity from the ratio of 1:1 to 1:5. An increase in the dCN concentration distorted the crystalline structure of α-Bi_2O_3, possibly through the formation of Bi-N interfacial bridges. The change in crystal structure is associated with the change of atom arrangement in the lattice of the materials. This influences properties like internal electric field, charge transfer, light interaction, catalytic active site exposure, and the overall performance of the material. Thus, in this work, the chemical interaction or crystal structural change observed could be vital for photocatalytic performance by realizing high reparation of charge carriers.

The vibrational and interaction attributes of the photocatalysts were investigated using Raman spectroscopic analysis, shown in Figure 1c. The Raman spectrum of MBO displays the typical Raman characteristics of α-Bi_2O_3, as described elsewhere.[49] In brief, the vibrational and rotational modes are classified based on their frequencies. As such, there are low-frequency Raman modes (30–70 cm^{-1}), heavy metal ion vibrations (70–150 cm^{-1}), intermediate bridged anion vibrational modes (300–600 cm^{-1}), and nonbridging anion vibrational modes (>600 cm^{-1}).[50] Most of the vibrations in this material come from Bi and O atoms, and the data is in accordance with the literature and XRD analysis. On the other hand, the Raman spectrum of unadulterated dCN displays the typical carbonaceous material characteristics, with D, G, and 2D bands located at 1366, 1580, and 2741 cm^{-1}, respectively.[51,52] The D-band (Raman-based disorder signature) emanates from sp^2 carbon atoms, while the G-band (prominent Raman-allowed first-order) arises from disorder and defects in the sp^3 carbon atoms.[52,53] Moreover, the 2D band (second-order) suggests that the produced graphitic carbon nitride has a similar resemblance to graphene with a double bond resonance process linking phonons to the electronic structure.[54] The intensity of the D-band, which emanates primarily due to double-resonance Raman scattering, provides important information about the amorphousness of carbonaceous materials, and the strong intensity compared to that of the G-band suggests that the sample is amorphous. This result coincides with the XRD analysis. Similar results have been reported by other researchers for carbon-rich graphitic carbon nitride obtained via a citric acid-mediated synthesis route.[51,53] The D-to-G band intensity (I_D/I_G) ratio was calculated to evaluate the defect severity and degree of distortion in the dCN and was found to be 1.20, which confirmed additional defects. After compositing MBO and dCN, the intensity and number of the MBO bands decreased, signifying the chemical interaction of the materials, which resulted in the emergence of a new band at approximately 601 cm^{-1} in the 1:1, 1:3, and 1:5 composites. This band could be the result of Bi-N bond formation, which is similar to what was recently reported by Yue et al.[55] Coincidental to the Raman spectra of the 1:1, 1:3, and 1:5 composites, new peaks are observed at approximately 627 and 579 cm^{-1} in the IR spectra of the specified composites (Figure S1a, Supporting Information); these peaks are linked to the formation of Bi-N bridges.

The surface and internal morphology together with the elemental composition were studied using SEM and TEM. An image of MBO in Figure 1d shows that the microrods were decorated with evenly distributed particles of different shapes and sizes. Figure 1e shows the morphology of the dCN alloy bearing a mixture of sheets and tubes, revealing the typical morphology of graphitic carbon nitride. The formation of the MBOdCN composite is shown in Figure 1f, and the morphologies of MBO and dCN confirm the formation of a heterostructured material. Furthermore, the TEM image of MBO revealed microrods covered by small squares and irregularly shaped particles, similar to the SEM image (Figure 1g). Moreover, in the case of dCN, the TEM image showed thin irregularly shaped sheets with ruptured tubes (Figure 1h). The MBOdCN TEM image shown in Figure 1i is composed of a mixture of irregular shapes and sheets of MBO and dCN, which is similar to the SEM image. Furthermore, the HRTEM image of MBOdCN shows amorphous dCN at the periphery and an MBO lattice fringe of 0.33 nm corresponding to the (120) crystal plane of Bi_2O_3 (Figure 1j).[18] Similar crystal plane is shown in the live profile image in Figure S2 (Supporting Information). In addition, the confirmation of the elemental composition is depicted in Figure 1k, as EDS mapping of the MBOdCN material reveals the uniform distribution of Mg, Bi, C, N, and O elements in the material, further confirming phase

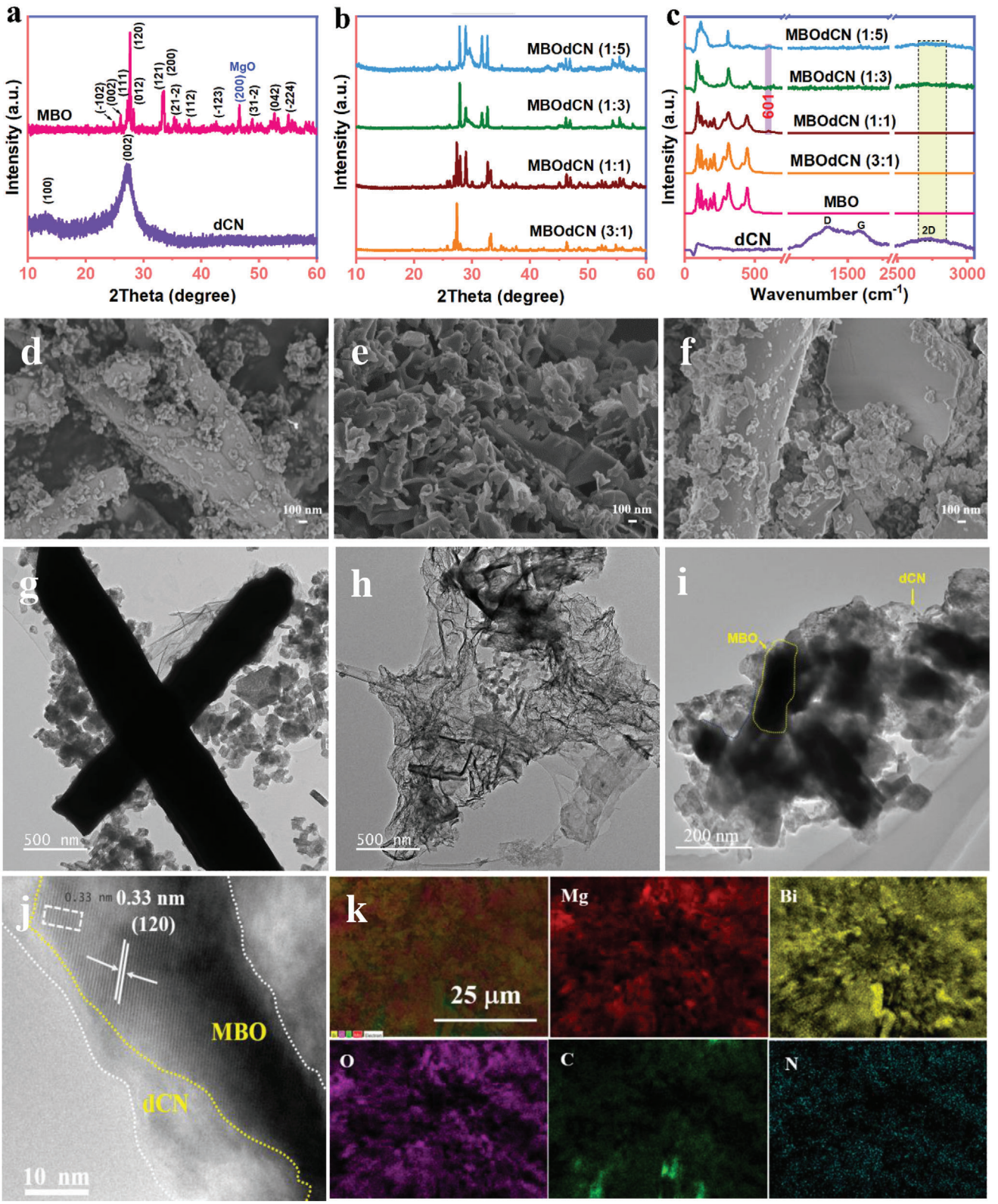

Figure 1. a,b) X-ray diffraction (XRD) diffractograms, c) Raman, SEM, and TEM micrographs of d,g) MBO, e,h) dCN, and f,i) MBOdCN; j) HRTEM image; and k) EDS elemental mapping image of the MBOdCN photocatalyst.

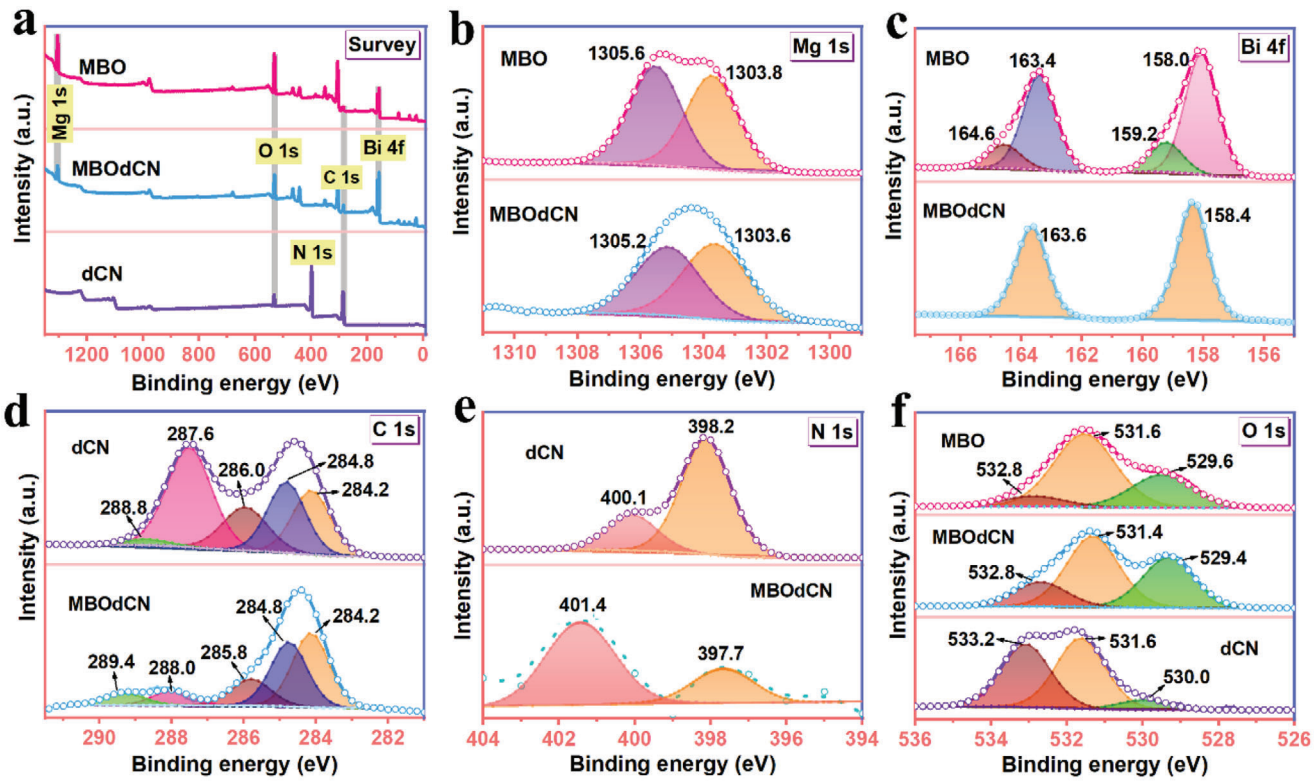

Figure 2. a) X-ray photoelectron spectroscopy (XPS) survey spectra, b) Mg 1s, c) Bi 4f, d) C 1s, e) N 1s, and f) O 1s high-resolution spectra of MBO, dCN, and MBOdCN photocatalysts.

purity, homogeneity, and uniform interfacial contact between the MBO and dCN materials.

The chemical environment, charge transfer, and oxidation states were investigated by XPS, as indicated in **Figure 2**. The XPS survey scans in Figure 2a display the expected elements, such as Mg, Bi, O, C, and N, for MBO, dCN, and the MBOdCN composite. Evidently, no impurities were detected, indicating the high purity of the prepared samples. The spin splitting of Mg 1s is shown in Figure 2b, with two prominent peaks at 1305.6 and 1303.8 eV for MBO, while they downshifted to 1305.2 and 1303.6 eV in MBOdCN. These peaks indicate the presence of the Mg^{2+} state, which was also revealed by XRD analysis.[56] The Bi 4f splitting orbital of MBO (Figure 2c) displays small peaks at 164.6 eV (Bi $4f_{5/2}$) and 159.2 eV (Bi $4f_{7/2}$) and more intense peaks at 163.4 eV (Bi $4f_{5/2}$) and 158.0 eV (Bi $4f_{7/2}$). The spectrum reveals the coexistence of Bi^{5+} (small peak) and Bi^{3+} (intense peak) oxidation states.[57,58] In the spectrum of MBOdCN, the Bi^{3+} peak upshifted to 163.6 and 158.4 eV, respectively. The high-resolution XPS spectrum of C 1s is illustrated in Figure 2d, with peaks centered at 284.8 and 284.2 eV for both materials, which represent sp^3 hybridized carbons (C–C) and adventitious sp^2 hybridized carbons (C=C), respectively. The peaks situated at binding energies of 288.8, 287.6, and 286.0 eV indicated the presence of C–C=O/C–N–C, C–$(N)_3$/N=C–NH_x, and C–OH, respectively.[48,59] In the MBOdCN comparison, these three peaks shifted, and their intensities decreased. The N 1s spectrum (Figure 2e) shows peaks centered at 400.1 and 398.2 eV for dCN; these peaks are upshifted (401.4 eV) and downshifted (397.7 eV) in the MBOdCN materials. These are linked to amino functionalities (C–N–H) and the sp^3 hybridized N atom in the triazine ring (C=N–C), respectively. Finally, Figure 2f shows the high-resolution XPS spectrum of O 1s, with MBO peaks located at 532.8, 531.6, and 529.6 eV corresponding to hydroxyl groups, chemically adsorbed oxygen, and lattice oxygen (Bi–O/Mg–O), respectively. These peaks are located at 532.8, 531.4, and 529.4 eV in the spectrum of MBOdCN, most of which show a downward shift. In the O 1s spectrum of dCN, bands are observed at 533.2, 531.6, and 530.0 eV corresponding to adsorbed moisture, O–C–O, and C=O, respectively.[60] The above results confirmed the successful integration of MBO and dCN together, which was evident by a shift in peak positions to confirm changes in electron density. The upward shift in the Bi 4f binding energy signifies the loss of electrons and interactions with nitrogen pots to form Bi–N bonds. The upward shift of the Mg 1s peak is proof that Mg was doped into the crystal structure of α-Bi_2O_3, as indicated by the XRD analysis and the formation of intermediate Fermi states, thus reducing the normal bandgap energy of α-Bi_2O_3 from approximately 2.80 eV to 2.64 eV, as indicated by the Tauc plots. Some of the bonds receive electrons from Bi, and others pass them through to Mg, as indicated by the data. This kind of electron movement enhances the separation of charges and effective photocatalytic performance, as previously reported.[61]

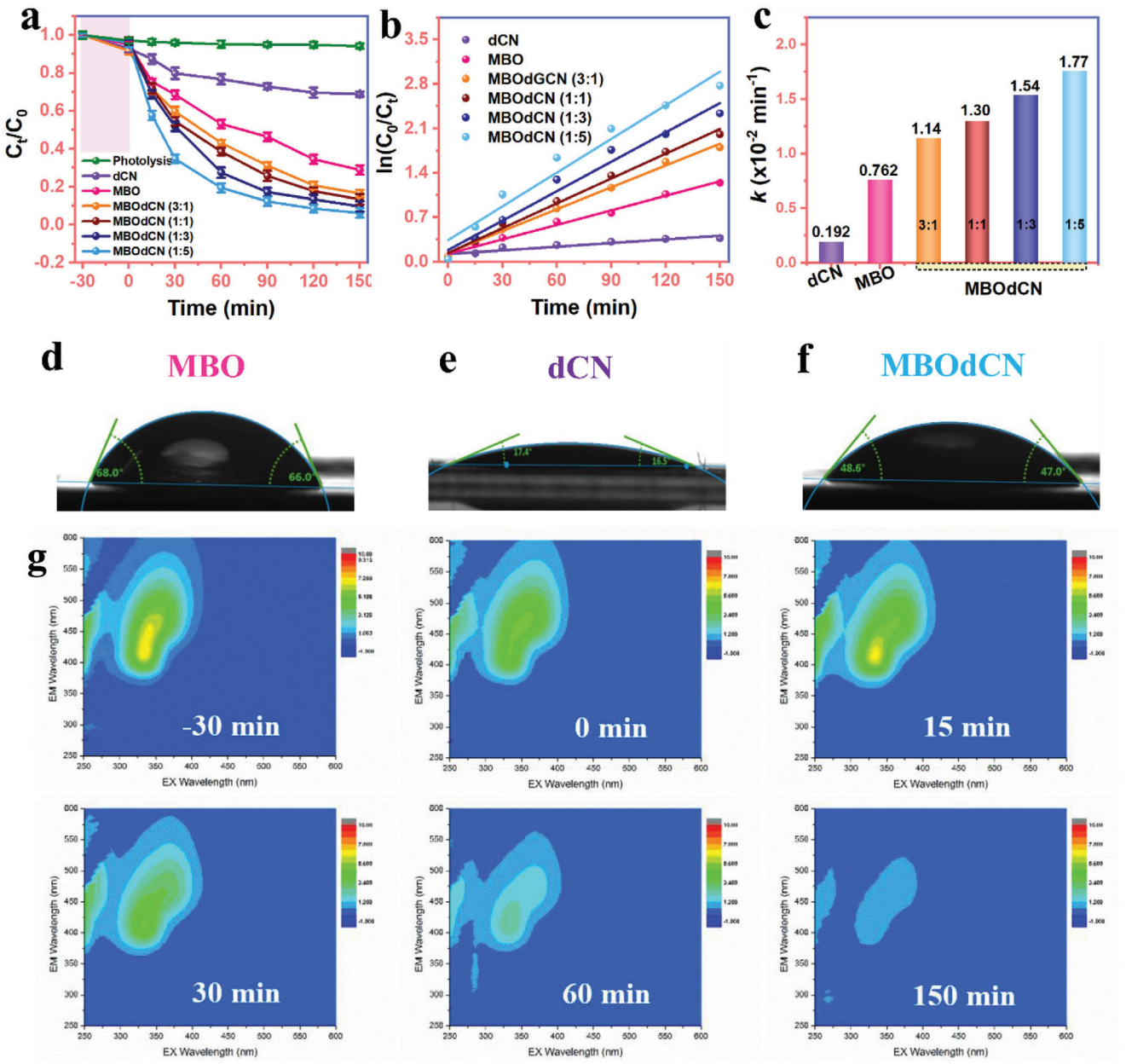

Figure 3. a) Photoactivity of different catalysts under visible light, b,c) kinetic data based on pseudo-first-order dynamics, d–f) contact angle measurements, and g) 3D excitation-emission matrix (EEM) spectra of oxytetracycline (OTC) solutions at different reaction times. Note: fluorescence excitation-emission matrices (FEEMs) at 90 and 120 min were left out because they did not show much difference.

2.2. Photocatalytic Performance of MBOdCN S-Scheme Photocatalyst

The photocatalytic performance of MBOdCN S-scheme nanostructures with varying MBO:dCN ratios (3:1, 1:1, 1:3, and 1:5) was investigated against OTC, a representative tetracycline antibiotic. Photoactivity evaluation experiments were conducted for 150 min under simulated solar light in the presence of 10 mg L^{-1} OTC aqueous solution (50 mL, pH = 6.32) and 20 mg of the composite photocatalysts as well as MBO and dCN as control samples. In the absence of a photocatalyst, simulated solar light could not degrade OTC, as this pollutant is very stable and hard to self-degrade under simulated solar light only (**Figure 3a**). Again, Figure 3a shows that after 30 min of contact time between the catalysts and the OTC solution in the dark, the percentage of the adsorbed antibiotic drug was less than 10%, which indicates a fairly low adsorption capacity. Upon simulated solar light irradiation, OTC degradation increased from 31.70% in the presence of dCN to 71.15% when MBO was used as the catalyst. Predictably, the heterojunction photocatalysts showed significantly greater OTC degradation efficiencies than the individual materials (MBO and dCN). This is an indication of the positive influence of coupling the two materials, which resulted in synergistic effects and overall improvement in OTC removal. Specifically, OTC

degradation increased remarkably with increasing dCN loading from 86.60% for MBOdCN (1:1) to a maximum degradation of 93.76% for MBOdCN (1:5), which had the highest dCN precursor loading. Intriguingly, increasing the MBO loading relative to that of dCN yielded lower OTC degradation, which was approximately 83.51% for MBOdCN (3:1) compared to approximately 90.35% attained using MBOdCN (1:3). This signifies the importance of the design and selection of the base catalyst and modifying material, as well as their composition in the heterojunction. Generally, the ratio of the components of heterojunction photocatalysts must be adjusted to ensure adequate interaction and intimate contact, which favors charge separation and transfer. Ultimately, this leads to synergy between the materials, leading to an overall improvement in photocatalytic activity. OTC degradation was further studied using pseudo-first-order kinetics (Figure 3b) to determine the apparent rate constants in the presence of the different catalysts. As expected, MBO and dCN showed lower degradation rates compared to other heterostructures owing to the prevalent recombination of photogenerated charge carriers, among other shortcomings. Figure 3c indicates that the OTC degradation rate constant reached a maximum of 0.0177 min^{-1} for MBOdCN (1:5), which was 9.22 times and 2.32 times greater than that obtained in the presence of dCN and MBO, respectively. Compared to those of the other heterojunction photocatalysts, the apparent rate constant over MBOdCN (1:5) was 1.55 times, 1.36 times, and 1.15 times superior to the OTC degradation rates recorded in the presence of MBOdCN (3:1), (1:1) and (1:3), respectively. As a result, MBOdCN (1:5) was selected as the working catalyst for detailed characterization and evaluation of the influence of various experimental conditions during OTC degradation.

One of the prerequisites for the efficient photocatalytic performance of a catalytic material is its interaction with water-containing pollutants. As such, the contact angles of the MBO, dCN, and MBOdCN samples were measured to evaluate their wetting properties (Figure 3d–f). All the samples had contact angle values lower than 90° which is an indication of good hydrophilicity. The dCN material displays the smallest contact angle which could be due to the presence of more hydroxyl groups from tannic and cyanuric acids.[60] The values showed that interactions between the catalyst surface and pollutants in water would not be prejudiced, as would be the case for hydrophobic surfaces with contact angles more than 90°.

The 3D fluorescence excitation-emission matrix (FEEM) was used to evaluate the photocatalytic effect of the MBOdCN catalyst on OTC (Figure 3g) for determining the aromaticity, aliphatic characteristics, and chemical composition of the treated water matrix.[62] The results for OTC before any process (−30 min) displayed two fluorescence peaks at approximately $\lambda_{Ex/Em}$ (250−260)/(370−500) and (300−420)/(360−550), with the second peak showing a more intense color. The observed fluorescence indicated the presence of a humic-like substance, which slightly decreased in the dark, suggesting the adsorption of OTC on the surface of the catalyst. When simulated solar light was applied for 15 min, the fluorescence peaks were reintensified, which could be attributed to the formation of new, smaller products and the detachment of OTC molecules from the catalyst surface. Further inspection revealed that the fluorescence peaks generally faded as time increased to 30 min and diminished further up to 150 min, signifying the photodegradation of the OTC structure. In particular, at reaction times of 60 and 150 min, $\lambda_{Ex/Em}$ (280−290)/(300−310) and (260−270)/(280−310) fluorescence peaks were observed, indicating the production of protein-like (tyrosine and tryptophan) substances that were initially not present. This is clear evidence of the gradual oxidation of OTC by the MBOdCN/simulated solar light system.[63]

The influence of the initial photocatalyst dosage, OTC concentration, and solution pH was systematically studied to explore their impact on the photocatalytic process, and the results are displayed in **Figure 4**. The effect of photocatalyst dosage on the photocatalytic degradation of fixed concentrations of OTC (10 mg L^{-1}) was evaluated using different quantities of the MBOdCN (1:5) catalyst (0.20, 0.40, 0.60, 0.80, and 1.00 g L^{-1}) and the results are shown in Figure 4a–c. When the photocatalyst concentration increased from 0.20 to 0.60 g L^{-1}, the OTC removal efficiency increased remarkably from 82.97% to 98.23% within 150 min of irradiation (Figure 4a). This significant improvement in OTC removal efficiency was ascribed to increased catalytic active sites and the production of reactive radicals presented by the increased amount of a catalyst. Nonetheless, further photocatalyst increases to 0.80 and 1.00 g L^{-1} led to decreased OTC removal of 96.42% and 92.01%, respectively. This phenomenon could be attributed to several factors, such as reduced accessibility of the catalyst active sites due to blockage by the excessive amount of photocatalyst, inhibition of light penetration due to increased opacity of the solution, and reduced separation of photogenerated charge carriers owing to the collisional contact between inordinate photocatalyst particles.[64] Collectively, these factors restricted the photocatalytic removal efficiency of OTC. As indicated in Figure 4b,c, the data was fitted with pseudo-first-order kinetics, and the rate of 0.60 g L^{-1} (0.0235 min^{-1}) was 1.81, 1.77, 1.14, and 1.58 faster than those of 0.20 (0.0130 min^{-1}), 0.40 (0.0177 min^{-1}), 0.80 (0.0206 min^{-1}), and 1.00 g L^{-1} (0.0149 min^{-1}), respectively. Therefore, the amount of catalyst was fixed at 0.60 g L^{-1} as the optimal quantity for further experimental execution.

Similarly, the influence of the OTC concentration was investigated using 10, 20, 30, 40, and 50 mg L^{-1} while the catalyst dosage was kept constant (0.60 g L^{-1}) (Figure 4d–f). The results showed that the OTC removal efficiency reached 98.23% within 150 min when the concentration was 10 mg L^{-1}. The OTC removal efficiency decreased from 98.23% to 82.61% when the concentration was increased to 50 mg L^{-1}. The decrease in efficiency was linked to the competition between the parent pollutant and intermediates for catalytic active sites, an increase in the number of OTC molecules that could not be matched by the active sites availed by 0.60 g L^{-1} catalyst, and the inhibition of light penetration to the catalyst surface by the increase in the OTC concentration.[65] The rate constants for different OTC concentrations were obtained after using a pseudo-first-order model, and the results are shown in Figure 4e,f. Compared with the other concentrations, 10 mg L^{-1} OTC had the highest rate constant; thus, the OTC concentration was fixed at 10 mg L^{-1} for subsequent experiments.

Finally, as an influential parameter of the catalyst's surface charge, pollutant chemical properties, and reaction kinetics, pH was optimized systematically by studying three pH values (pH 2.78, 6.36, and 11.82), and the findings are illustrated in Figure S3a–c (Supporting Information). Interestingly, a change in pH was accompanied by an obvious shift in the wavelength

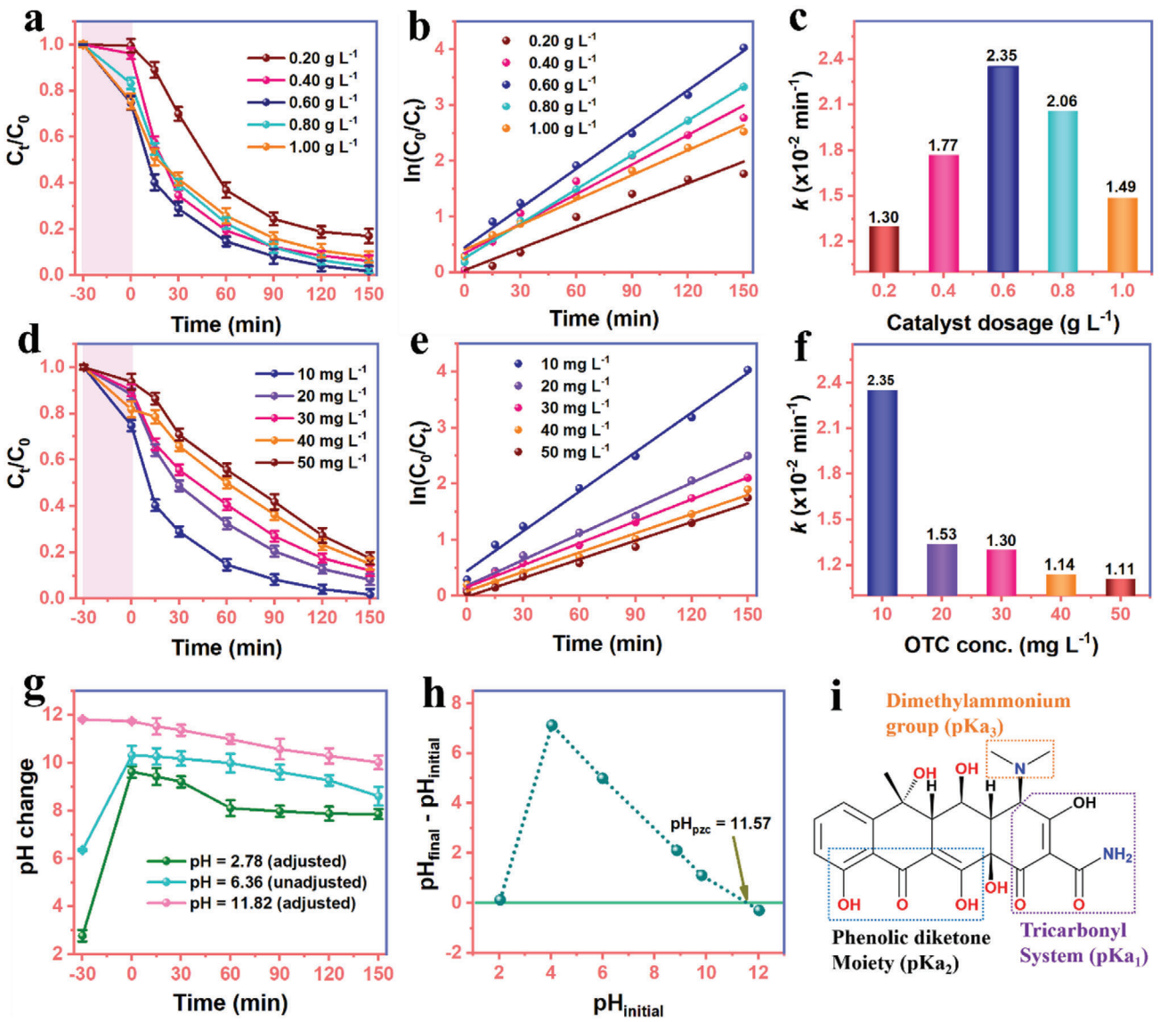

Figure 4. Effects of a–c) catalyst dosage and rate constants, d–f) initial concentration and rate constants of oxytetracycline (OTC), g) change in pH with increase in reaction time, h) pH_{pzc} of the MBOdCN catalyst, and i) pK_{as} of the OTC structure.

of maximum absorption for both pronounced peaks of OTC, which could be influenced only by changes in charge on both the catalyst and the pollutant as the photocatalysis process proceeded. Specifically, at pH 2.78 and 6.36, there was a blueshift in the wavelength of maximum absorption immediately after the adsorption–desorption process in the dark (Figure S3a,b, Supporting Information). In contrast, at pH 11.82 there was no peak shift observed as can be observed in Figure S3c (Supporting Information). These blueshifts could be linked to the changes in catalyst surface charge and pollutant upon interaction, which could have consumed H^+ ions to shift the pH to the alkaline range. Figure 4g shows the change in pH during the photocatalytic degradation of OTC. Evidently, blueshifts were observed during a change in pH from acidic to alkaline (above pH 7), where OTC was effectively photodegraded. Figure 4h,i displays information on the catalyst point of zero charge (pH_{pzc} 11.57) and the speciation of OTC with pK_{as}. As observed from Figure 4g, photocatalytic degradation occurred in an alkaline solution where the catalyst surface was mostly positively charged. Moreover, OTC was dominated by negatively charged $HOTC^-$ and OTC^{2-} species, thus leading to electrostatic attraction between the catalyst and the pollutant. As established elsewhere,[66] at pH 3.0 to 5.5, the most predominant OTC species are H_3OTC^+ and H_2OTC, and minor species such as $HOTC^-$ are also present. Between pH 7.0 and 8.5, H_2OTC and $HOTC^-$ were the predominant species, while the minor species included H_2OTC and OTC^{2-}. Finally, from pH 10.0 to 11.0, OTC^{2-} and $HOTC^-$ were the only OTC species present. At all three pH values studied, the degradation efficiencies obtained were 93.68 (pH 2.78), 98.23 (pH 6.36), and 99.56% (pH 11.82), and the findings are comparable to those of other reports.[64,67–69] Therefore, a pH of 11.82 was adopted for the subsequent reaction as the optimal value.

Table 1. Comparison of MBOdCN performance with other reported catalysts toward the degradation of oxytetracycline (OTC) under visible light and different photocatalytic systems.

Photocatalyst (E_g)	Reaction conditions	Light source	Efficiency[[%]	Rate [min^{-1}]	Energy consumption [kWh m^{-3}]	Refs.
MBOdCN (2.11 eV)	[Catalyst] = 0.6 g L^{-1}, [OTC] = 10 mg L^{-1} (50 mL), pH = 11.82, Time = 150 min, System = S-scheme	Visible light (300 W Xe lamp, $\lambda > 420$ nm)	99.56	0.02346	6.37	This work
BTO@Bi_2S_3/PU (2.996 eV)	[Catalyst] = 1 cm × 1 cm × 1 cm × 12 [OTC] = 10 mg L^{-1} (50 mL), Current = 20 mA, pH = 5.58, Time = 180 min System = Z-scheme	Visible light (300 W Xe lamp)	82.08	0.00785	24.11	[71]
BiOI(001)/CdS (N/d)	[Catalyst] = 1 g L^{-1} [OTC] = 24 mg L^{-1} (50 mL), pH = N/d, Time = 30 min System = Z-scheme	Visible light (300 W Xe lamp, $\lambda > 420$ nm)	90.3	0.0711	2.96	[72]
4BN-$BiVO_4$ (2.47 eV)	[Catalyst] = 0.4 g L^{-1}, [OTC] = 30 mg L^{-1} (50 mL), pH = 7, Time = 120 min, System = N/d	Visible light (350 W Xe lamp, $\lambda > 420$ nm)	77.4	0.0138	21.68	[73]
Cu_3P/BiOCl-1.5 (N/d)	[Catalyst] = 0.5 g L^{-1}, [OTC] = 20 mg L^{-1} (50 mL), pH = N/d, Time = 6 min, System = S-scheme	Visible light (300 W Xe lamp)	86	0.216	0.70	[74]
Bi/Bi_2S_3/Bi_2WO_6 (2.18 eV)	[Catalyst] = 1 g L^{-1} [OTC] = 30 mg L^{-1} (30 mL), pH = N/d, Time = 15 min, System = S-scheme	Visible light (300 W Xe lamp, $\lambda > 420$ nm)	84.3	N/d	3.11	[75]
g-C_3N_4/BiOCl/CdS (1.54 eV)	[Catalyst] = 0.25 g L^{-1}, [OTC] = 10 mg L^{-1} (200 mL), pH = 7, Time = 240 min, System = Z-scheme	Visible light (15 W) Sunlight	87.0 99.3	0.01644 0.02293	0.34	[2]
CoFe@NSC-1000 (1.28 eV)	[Catalyst] = 0.3 g L^{-1}, [OTC] = 50 mg L^{-1} (40 mL), pH = 4, Time = 150 min, System = Z-scheme	Visible light (300 W Xe lamp, $\lambda > 400$ nm)	90.0	0.01111	18.75	[76]
Bi/BiOBr/$Bi_2O_2CO_3$ (N/d)	[Catalyst] = 1 g L^{-1} [OTC] = 50 mg L^{-1} (50 mL), pH = N/d, Time = 60 min, System = Type-II	Visible light (300 W Xe lamp, $\lambda > 420$ nm)	70.23	0.0225	11.40	[77]
GCNQDs-$CoTiO_3$/$CoFe_2O_4$ (1.91 eV)	[Catalyst] = 0.6 g L^{-1}, [OTC] = 40 mg L^{-1} (50 mL), pH = 7, Time = 150 min, System = Z-scheme	Visible light (500 W Xe lamp, $\lambda >$ N/d)	88	0.01409	27.15	[78]

N/d = Not disclosed.

It is a universal practice to compare the performance of the prepared photocatalyst to other materials reported in the literature for OTC degradation. Therefore, the MBOdCN catalyst was compared to other reported photocatalysts for the degradation of OTC under visible light. It is observed different parameters such as light power, degradation time, efficiency, volume, pH, and catalytic mechanism could greatly influence the degradation of OTC by different photocatalysts. Moreover, the cost of the degradation process was determined using energy consumption (kWh m^{-3}) as the IUPAC figure of merit, and the values were compared with other reported work.[70] Equation (1) was used to determine the values as indicated below:

$$EC = \frac{Pt}{\log\left(\frac{C_0}{C_t}\right) \times V} \quad (1)$$

Here P represents Xe lamp power consumption (kW), t is the reaction time (h), V is the volume (L), and C_0 and C_t are the initial and final concentrations of OTC (mg L^{-1}), respectively. The energy consumption of OTC degradation by MBOdCN was found to be 6.37 kWh m^{-3} and was comparatively lower than other reports. This value is also 59.65 times lower than the energy consumption of conventional wastewater treatment (380 kWh m^{-3}) in South Africa. Thus, with the observation it can be concluded that the longer the degradation time the higher the energy consumption by the system. The results obtained with this catalyst are comparable to those reported in the literature as depicted in **Table 1**. This indicates the potential for exploring the material in the degradation of tetracyclines and other pharmaceutical drugs in the aquatic environment.

2.3. Optical and Photoelectrochemical Properties

The optical properties of the materials were studied by UV–Vis DRS, XPS-VB, and photoluminescence (PL) analyses while electrochemical techniques were used to evaluate charge transfer

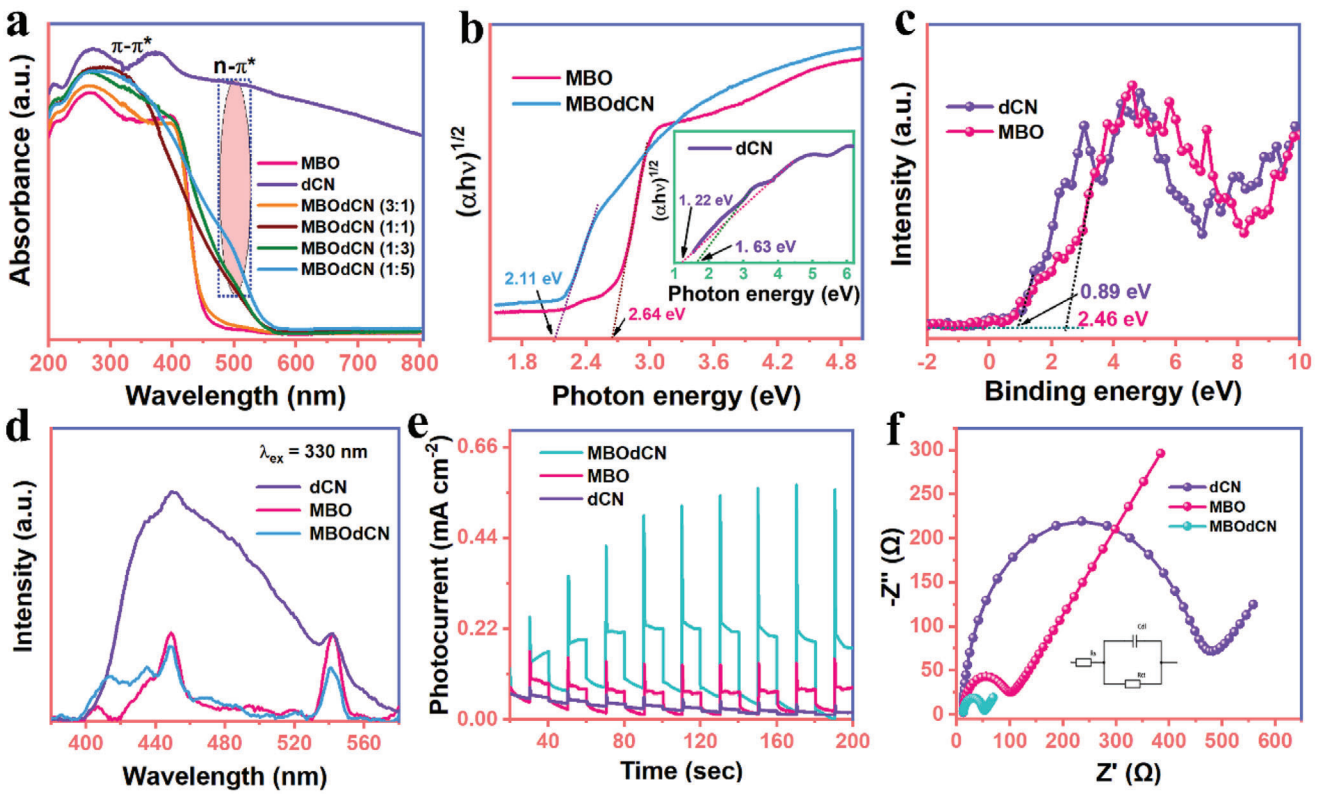

Figure 5. a) UV–Vis DRS spectra, b) Tauc plots, c) X-ray photoelectron spectroscopy (XPS) valence band (VB) spectra, d) photoluminescence (PL) spectra, e) photocurrent measurements, and f) electrochemical impedance spectroscopy (EIS) (inset: equivalent Randle circuit fit) data of the materials.

within the materials (**Figure 5**). The DRS spectrum of MBO displays an absorption edge at approximately 447 nm with bands in the UV region emanating from charge transfer between oxygen and metals (Figure 5a). Pristine dCN displays more visible light absorption with distinct bands at approximately 273 and 373 nm, which are due to the $\pi-\pi^*$ electronic transitions from the C═N groups in the conjugated tri-s-triazine units.[51] The other band at approximately 507 nm is linked to the n$-\pi^*$ electronic transitions of amine or heptazine nitrogen lone pairs, indicating the existence of an additional electronic transition pattern.[67] In particular, the composites with more dCN content show more visible light absorption and n$-\pi^*$ electronic transitions, proving that the material consists of MBO and dCN. In Figure 5b, the bandgap energies of MBO, MBOdCN, and dCN (inset) were determined to be 2.64 (approximately 2.80 eV for Bi_2O_3),[18] 2.11, and 1.63 eV, respectively. The theoretical bandgap energies were found to be 2.63, 1.64, and 2.14 eV for MBO, dCN, and the MBOdCN S-scheme heterostructure (Figure S4a–c, Supporting Information). This indicated that the HSF06 functional group could validate the individual structures' and heterostructures' experimental bandgap values. Furthermore, more details on the total density of states (TDOS) and partial density of states (PDOS) are given in Text S5 (Supporting Information). The XPS valence bands (XPS-VBs) of MBO and dCN are depicted in Figure 5c. These values are 0.06 times less than the actual valance band of photocatalytic materials.[61] Therefore, the actual values of VBs of MBO and dCN were determined using the XPS-VB values and were found to be 2.52 and 0.95 eV, respectively. These VB values were used in combination with the bandgap energies to calculate the conduction band (CB) potentials of MBO and dCN and were found to be −0.13 and −0.68 eV, respectively. The calculated potentials were used for further discussions of photocatalytic mechanistic charge transfer.

The PL spectra of the pristine and composite materials are displayed in Figure 5d. The MBO PL spectrum shows bands at approximately 407, 449, and 542 nm, linked to electronic transitions between oxygen and metals. Moreover, the dCN spectrum displays the most intense peaks at 450 and 542 nm, with a shoulder at 435 nm. In the case of MBOdCN, the PL spectrum resembled that of MBO due to its significantly greater content in the composite relative to that of dCN. However, compared to the spectra of the pristine materials, the MBOdCN spectrum has notably low-intensity peaks, which are directly related to the high separation of photoinduced charges and increased lifetime of the charge carriers within the heterostructured material. This property is vital for the efficient photocatalytic performance of the material.[79] Furthermore, the charge separation efficiency and light response ability were tested via transient photocurrent (TPC) measurements (Figure 5e). The photocurrent response of MBOdCN is greater than that of MBO and dCN. The reason is that the construction of a heterojunction between MBO and dCN greatly promoted the photoresponse and effectively inhibited a high rate of charge recombination while improving the overall photocatalytic process. Figure 5f illustrates electrochemical impedance spectroscopy (EIS) curves with the inset displaying an equivalent Randle circuit used to fit the data. EIS is often employed to study

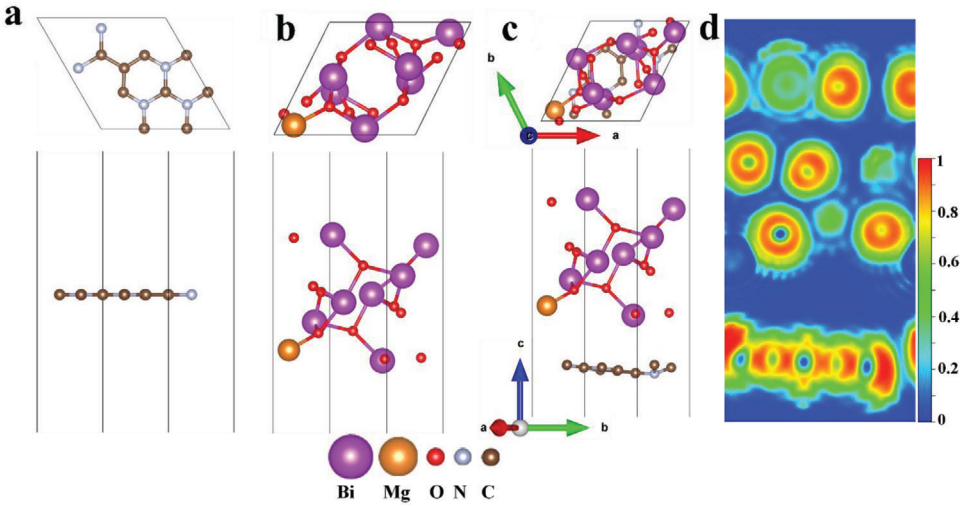

Figure 6. Top (above) and side (below) views of the optimized structure of a) dCN, b) MBO, c) MBOdCN heterostructure, and d) electron localization function (ELF) across the interface of MBOdCN heterostructure.

the charge resistance or transfer limitations within a material. MBOdCN exhibited the smallest arch radius in the EIS curve, revealing that the composite material suffered less of a hindrance to charge transport (395.44 Ω) compared to MBO (877.75 Ω) and dCN (1268.77 Ω), respectively.[80] Additionally, these findings indicate that additional photoinduced electrons and holes could be effectively utilized for photocatalytic OTC degradation. From the results of PL, TPC, and EIS, it is evident that heterojunction formation can considerably enhance the efficiency of charge separation and migration and minimize the rate of recombination. This approach is necessary for improving photocatalytic processes.

2.4. Optimized Structures of the Photocatalysts

The optimized crystal structures of dCN, MBO, and MBOdCN are shown in **Figure** 6a–c. The dCN is made up of carbon and nitrogen atoms while MBO indicates bismuth, oxygen, and magnesium in its structure. The MBOdCN heterostructure is constructed by stacking MBO and dCN on each other as indicated in Figure 6c. As illustrated in Figure 6d, the electron localization functions (ELFs) from the side view are projected in real space. The ELF ranges from 0 to 1, with 0 representing delocalized electrons, 0.5 representing the dispersion of electron-like gas or electron pairs, and 1 representing localized electrons.[81] Moreover, the results indicated the absence of electrons in the interfacial area, suggesting there was no binding there, which supports the vdW interactions in the MBOdCN heterostructure. However, other techniques, such as XRD, Raman, and FTIR, indicated the occurrence of binding between the MBO and dCN materials.

2.5. Charge Transfer and Mechanistic, and Pathway Analysis

The involvement and influence of various reactive species on the photocatalytic process were examined via scavenging experiments by employing p-benzoquinone (BQ), isopropyl alcohol (IPA), and ethylenediaminetetraacetic acid (EDTA) as quenchers of superoxide ($^{\bullet}O_2^-$), hydroxyl ($^{\bullet}OH$), and holes (h^+), respectively (**Figure** 7a). The introduction of BQ led to a high reduction in the photocatalytic efficiency of OTC, suggesting that $^{\bullet}O_2^-$ radicals play a predominant role. Again, a recognizable reduction was observed when EDTA and IPA were added to the photocatalytic system, confirming the secondary participation of the h^+ and $^{\bullet}OH$ radicals. Therefore, the order of photocatalytic contribution is $^{\bullet}O_2^- > h^+ > {}^{\bullet}OH$. To further ascertain the formation of the reactive species, electron-spin resonance (ESR) was performed to detect $^{\bullet}O_2^-$ and $^{\bullet}OH$ radicals formation in the presence of the composite catalyst under simulated solar light (Figure 7b,c). In the dark, no radicals were detected, suggesting that there is no possibility of charge generation in the absence of light. In contrast, $^{\bullet}O_2^-$ and $^{\bullet}OH$ radicals were strongly detected when the catalyst was irradiated with simulated solar light for 5 min, indicating the importance of the simulated solar light responsiveness of the catalyst for generating the required radicals for the photocatalytic process, as already indicated by the photocurrent response. Thus, a combination of quenching experiments and ESR revealed the importance of photogenerated radicals and can be used to determine the type of heterojunction formed.

Furthermore, the calculations of the electrostatic potentials and charge density differences were performed to examine the interfacial interactions in the MBOdCN heterostructure. The charge redistribution at the interfacial region of the MBOdCN heterostructure is caused by the difference in work functions between the component layers. The planar-averaged electrostatic potentials of MBO and dCN layers, as well as that of the MBOdCN were obtained to study the charge transfer process at the interfaces. The work function values of dCN and MBO are 4.02 and 4.97 eV as illustrated in Figure 7d,f. These values confirm that dCN loses electrons more readily than MBO does. This is consistent with the results of the charge density difference analysis. Henceforth, dCN acts as a p-doped component, and MBO acts as an n-doped component. The work function of MBOdCN is 4.43 eV as a result of the tendency of electrons to drive from dCN to MBO until the Fermi energy level becomes equal (Figure 7g). Subsequently, holes and electrons accumulate at dCN and MBO,

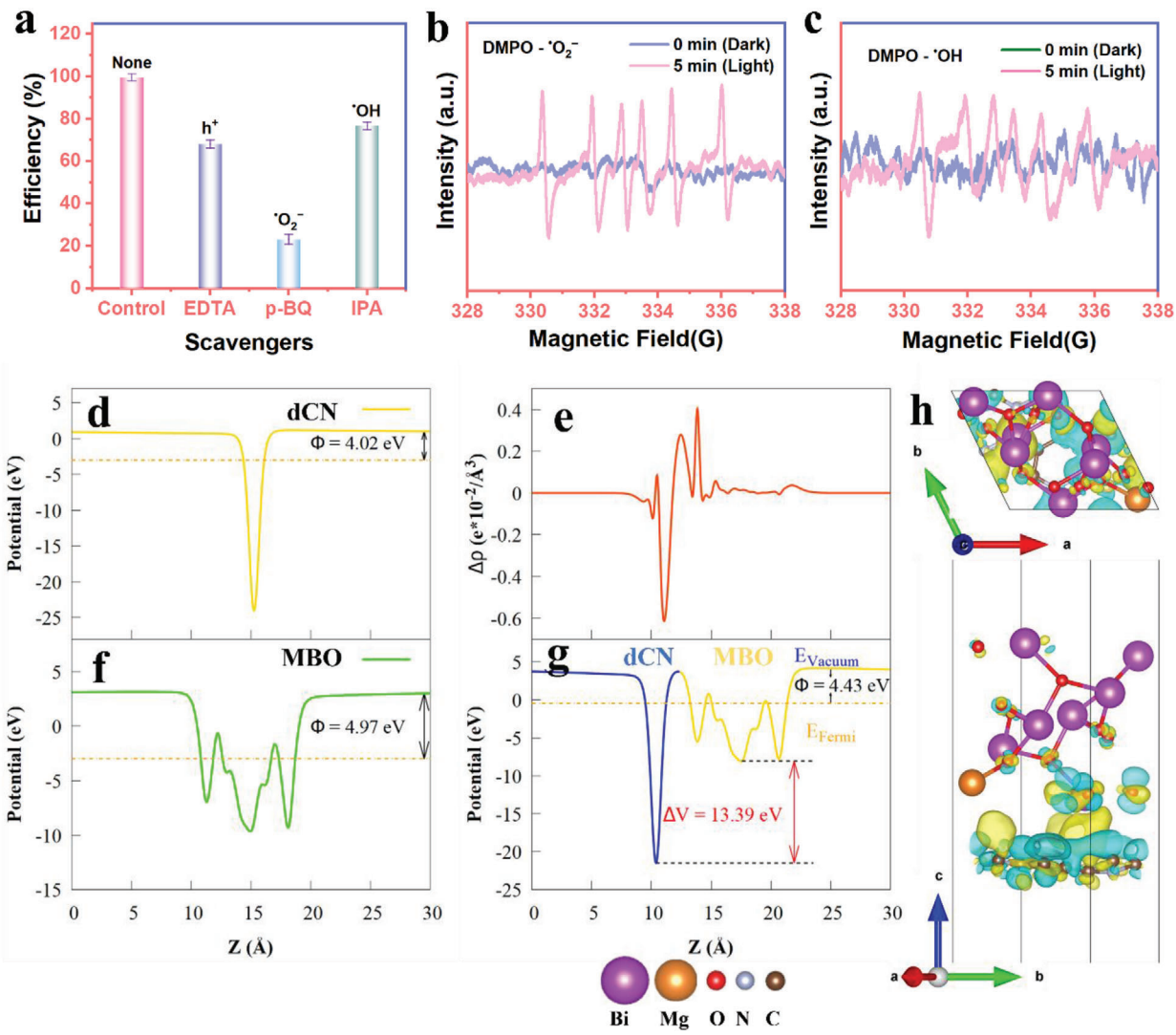

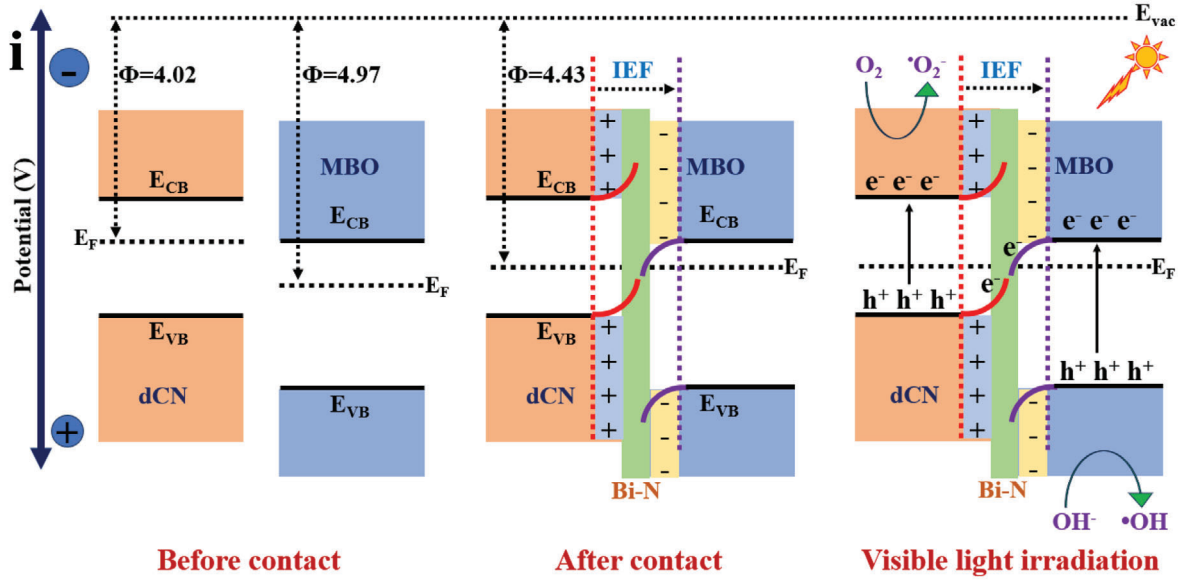

respectively. This accumulation creates a BIEF from the dCN to MBO. The variation in the work functions of the layers is the major cause of the potential drop (ΔV) at the heterostructure interface. With that, it was discovered that there is a significant ΔV (13.39 eV) at the interface, which can successfully prevent the reunion of photo-created electron–hole pairs in the MBOdCN, thus increasing the effectiveness of solar energy conversion. On the other hand, the charge transfer within the heterostructure was examined using the plane-averaged and three-dimensional (3D) isosurfaces of the charge density difference (Figure 7e,h). The charge depletion and accumulation are symbolized by the blue and yellow isosurfaces, respectively.[81] The dCN loses electrons (blue area), and MBO gains electrons (yellow area) when the charge is redistributed at the interfacial contact (Figure 7h), further demonstrating that the electrons have transferred from dCN to MBO. The charge redistribution in dCN is more pronounced than in MBO at the interface region. Using Bader charge analysis, interlayer charge transfer was quantified, and 0.069 |e| was found to be transferred from dCN to MBO, which is compatible with the CDD findings. Therefore, this proves that the transfer of photoinduced electrons occurred from dCN to MBO in the heterostructure, thus creating a BIEF.[82] The results are paving the way for the construction of a possible degradation mechanism in the MBOdCN/simulated solar light system.

Based on the obtained results and work functions of MBO (4.97 eV), dCN (4.02 eV), and MBOdCN (4.43 eV) (Figure 7d,f,g), a plausible photocatalytic charge generation and migration pathway for MBOdCN is constructed and shown in Figure 7i. The individual materials are shown with their band position alignment and work functions. When MBO and dCN get into contact with each other in the dark, Fermi level (E_F) equilibration is attained through the transfer of electrons from dCN due to its smaller work function and higher E_F to MBO with a larger work function and lower E_F. This phenomenon causes the upward curving of the dCN energy bands, signifying the occurrence of electron depletion, while the upward curving of the MBO curve indicates the accumulation of electrons. During the processes of upward and downward band curving, an interface forms between the two materials, giving rise to a BIEF from electron-deficient dCN to electron-rich MBO in the heterojunction. It is worth noting that the strong intimate linkages created by the Bi-N bonds serve as electron bridges and pathways for expediting electron migration from MBO to dCN down the electron concentration gradient. Ultimately, this leads to restriction, thereby retarding charge recombination and enhancing the S-scheme charge transfer route. Upon visible light exposure, the BIEF together with the bend-curving phenomenon initiates prompt migration of electrons from the CB of electron-rich MBO down the gradient and through the Bi-N bridges to combine with holes in the VB of dCN. This guarantees the maximum photoredox ability of the system while generating sufficient amounts of the reactive species ($^{\bullet}O_2^-$, h^+, $^{\bullet}OH$) on the CB of dCN and the VB of MBO for photocatalytic degradation of OTC.

As mentioned, the VB of dCN is +0.95 eV, while the CB of MBO is −0.13 eV; therefore, it is not energetically and thermodynamically favorable to oxidize OH^- to hydroxyl ($^{\bullet}OH$) radicals or reduce O_2 to superoxide ($^{\bullet}O_2^-$) radicals due to the high potential of $OH^-/^{\bullet}OH$ (+2.40 eV versus NHE) and more negative potential $O_2/^{\bullet}O_2^-$ (−0.33 eV versus NHE), respectively.[83] Thus, the hole in the VB of dCN and electrons in the CB of MBO are annihilated. On the other hand, the CB electrons in dCN have a high ability to reduce O_2 to $^{\bullet}O_2^-$ radicals (−0.68 eV), and at the same time, the oxidation of the MBO VB (+2.52 eV) can convert OH^- groups to $^{\bullet}OH$ radicals. These radical species ($^{\bullet}O_2^-$ and $^{\bullet}OH$) were confirmed to be the major participants in the destruction of OTC. The production of these radicals in this novel MBOdCN S-scheme system stems from the illumination of the photocatalyst with appropriate energy. The photoinduced electrons in MBO migrate via two channels for efficient isolation from their holes and migrate to the VB of dCN. In the first path, electrons are trapped by Mg sinks that were revealed by XPS to accept electrons, and their presence was confirmed by the reduction in the bandgap of Bi_2O_3. The second electron transfer path occurs via the Bi-N bridges formed at the interface, as confirmed by Raman and FTIR spectroscopy. This process contributes to an increase in the lifetime of the charge carriers and enhances their redox capabilities, as depicted in **Figure** 8a. Additionally, it is worth mentioning that the holes also participated in OTC degradation via direct oxidation, as shown by trapping experiments. This heterojunction constructed between MBO and dCN followed an S-scheme pathway of the charge transfer mechanism, leading to adequate separation of the photogenerated charge carriers and enhanced degradation of OTC into smaller molecules.

Subsequently, high-performance liquid chromatography time-of-flight-tandem mass spectrometry (HPLC-TOF-MS/MS) was used to identify the DP or intermediate in the MBOdCN/vis system for OTC elimination and the results are displayed in Figure S7a–c (Text S5, Supporting Information). Based on the mass-to-charge ratio (m/z) peaks, the degradation of OTC was proposed to occur through three different pathways involving different processes such as hydroxylation, demethylation, deamination, etc. (Figure 8b). Pathway 1 indicates that OTC was attacked by reactive oxygen species and two processes occurred (ketonation and hydroxylation) to yield DP1 (m/z = 475) which also underwent dihydroxylation, deamination, and demethylation to produce DP2 (m/z = 350). The decarboxylation occurred on DP2 to produce DP3 (m/z = 302) and this byproduct was methylated, and dehydroxylated, and most of the double bonds in the rings were converted into a single bond hopeful through attack by holes. DP3 underwent ring opening and hydroxylation to produce DP5 (m/z = 118). In pathway 2, OTC was subjected to demethylation, dehydroxylation, and deamination to release DP6 (m/z = 362). Subsequently, DP6 underwent ring elimination and deamination to form DP7 (m/z = 275) which was further transformed into DP8 (m/z = 157) via ring elimination. Cleavage of one ring in DP8 followed by hydroxyl group addition led to

Figure 7. a) Free radical capture experiments, b,c) electron-spin resonance (ESR) spectra of DMPO-$^{\bullet}O_2^-$ and DMPO-$^{\bullet}OH$ for MBOdCN. Planar-averaged electrostatic potentials of d) dCN, f) MBO, and g) the MBOdCN heterostructure. The work function (ϕ) and potential drop (ΔV) are highlighted. e) The plane-averaged and h) 3D charge density difference of the MBOdCN heterostructure. Charge accumulation and depletion are depicted as blue and yellow regions, respectively, with the isosurface set to 0.00057 $Bohr^{-3}$. i) Fermi levels inducing charge generation and transfer tendencies in an S-scheme heterojunction.

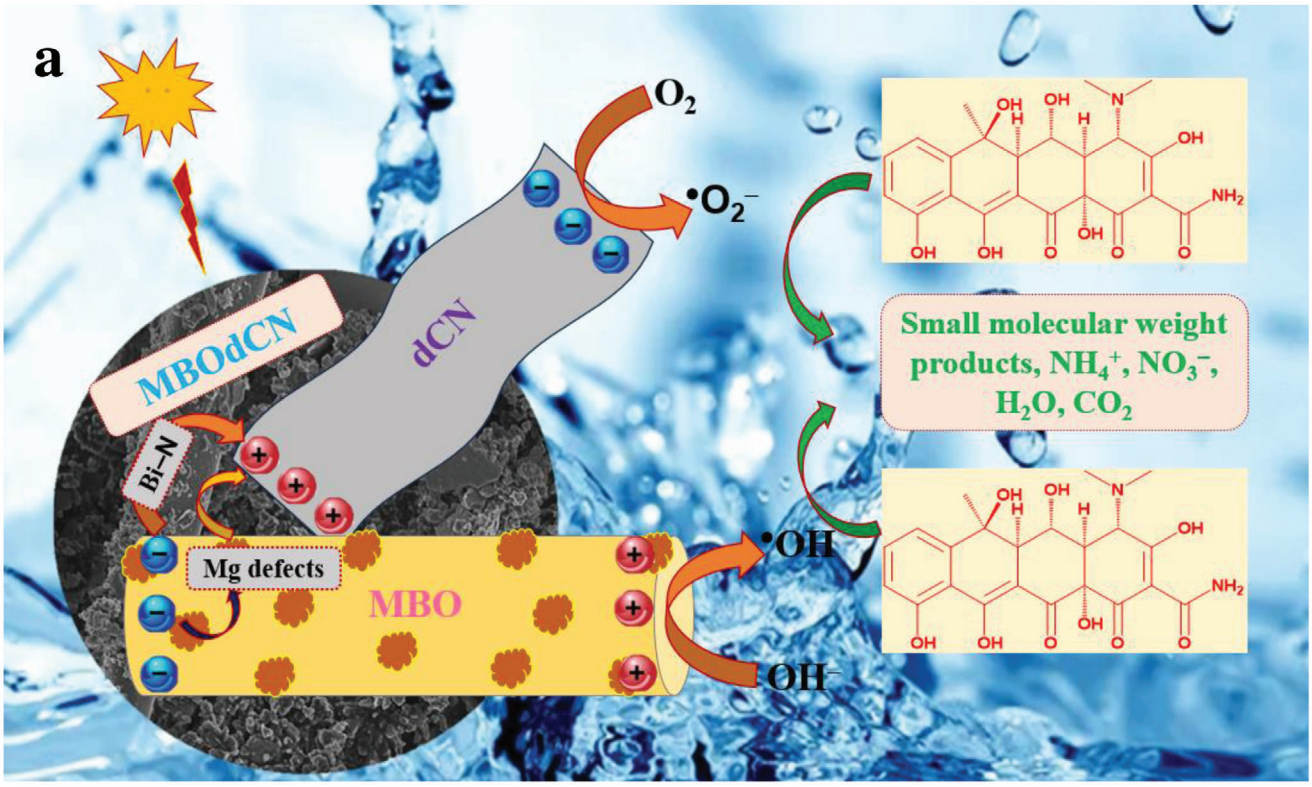

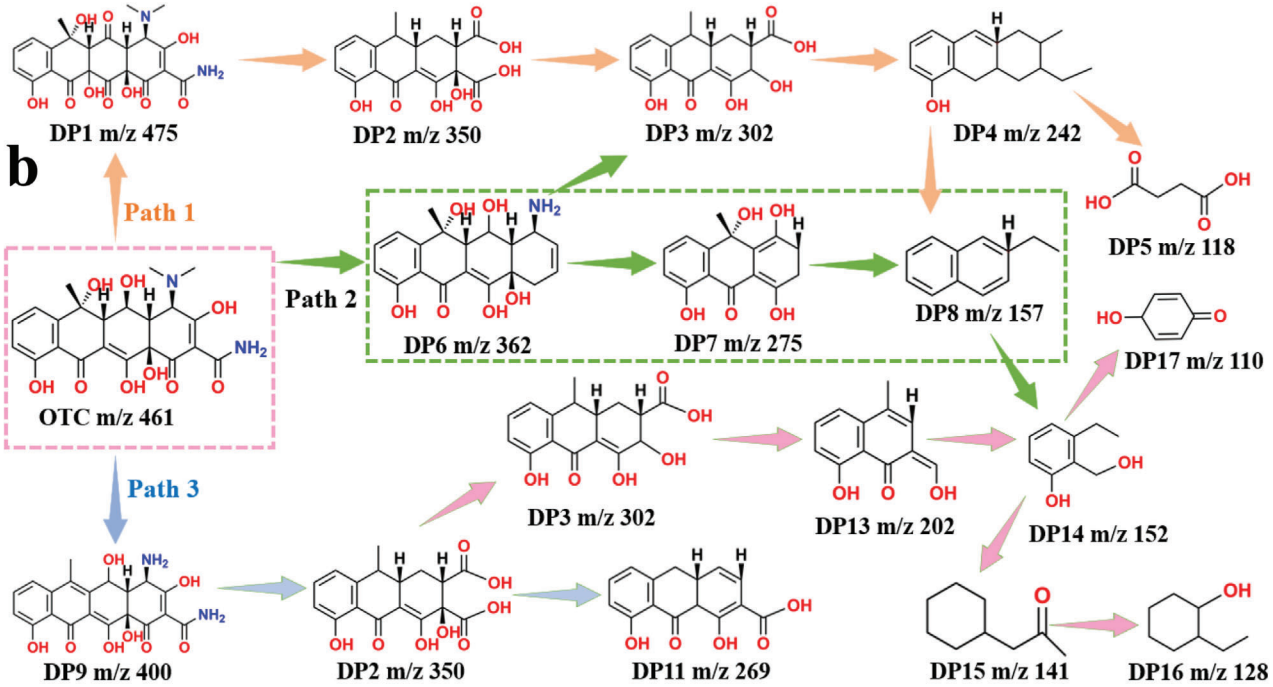

Figure 8. Schematic of the photocatalytic mechanism a) and degradation pathways b) of oxytetracycline (OTC) by MBOdCN/vis system.

DP14 (m/z = 152). In pathway 3, there was a loss of hydroxyl and N-methyl groups to generate DP9 (m/z = 400) which was further converted to DP2 via ring opening, deamination, and amide elimination reactions. DP2 in this pathway followed the pattern of pathway 1 with an addition of a split to yield DP11 via decarboxylation. DP3 in pathway 3 underwent ring elimination and carboxyl group removal to form DP13 (m/z = 202). Subsequently, more ring-opening reactions occurred, and hydroxylation and methylation led to the formation of DP14 (m/z = 152), DP15 (m/z = 141), and DP16 (m/z = 128). After 90 min of reaction (Figure S7c, Supporting Information), the dominant species was DP17 (m/z = 110) with only one ring showing the effectiveness of the MBOdCN/vis system toward OTC degradation. The smaller molecules could easily be mineralized into CO_2, H_2O, and other small inorganic molecules with further reactions.

For real-time applications, the stability of the photocatalyst is very important and has to be investigated thoroughly. The results of stability studies are given in Figure S6 (Supporting Information). The MBOdCN catalyst showed high stability where it exhibited OTC removal of 96.07% after five reuse cycles. The catalyst lost 3.48% of its efficiency toward OTC degradation. The XRD was used to study changes in patterns after the five cycles of reuse. The patterns display minor changes in the peak intensities of the used catalyst relative to those of the fresh material confirming the reasonable stability of the MBOdCN catalyst.

2.6. Cytotoxicity Assessment

Given the wide range of transformation byproducts produced by photocatalytic processes, it is essential to investigate how harmful are these byproducts to ecosystems to determine the practical application of the photocatalytic processes in water treatment. The epithelial cells that line the digestive system components play key roles in nutrient absorption, metabolism, digestion, and transport.[83] Additionally, water quality has a substantial impact on the epithelial lining of the intestines, which affects general human health and well-being. Therefore, evaluating the toxicity of the photocatalytic materials and the DP of pharmaceuticals is pivotal to the deployment of photodegradation techniques in water treatment. To this end, toxicity assessment via metabolic activity, lactate dehydrogenase (LDH) activity was investigated in normal cells (Kidney embryonic HEK293 cells) and epithelial cells (human intestinal Caco-2 cells), and hemolysis was assessed in erythrocytes from animal blood. As shown in **Figure 9**, the viabilities of the cells treated with the photocatalytic materials were all above 78%, even at concentrations as high as 1000 µg mL^{-1} (Figure 9a,b). Similarly, exposure of both cell lines to the OTC DP did not result in any noticeable reduction in viability (Figure 9c). As determined by the LDH assay, which is a proven biomarker for damaged cell membranes, all photocatalysts and the OTC byproducts evaluated exhibited similar patterns. Even at the highest concentration, the effective concentration (EC_{20}) was less than 20% in both HEK293 and Caco-2 cells and erythrocytes (Figure 9d–f). Although the toxicity, as measured by metabolic activity, was comparable to that determined by the LDH assay, the cytotoxicity, as measured by metabolic activity, was marginally greater than that determined by the LDH assay, suggesting disruption of mitochondrial stability rather than breach of the cell membrane.[84] Finally, treatment of erythrocytes with the photocatalysts resulted in hemolytic activity at increasing concentrations (Figure 9g) while OTC treatment also had the greatest degree of hemolytic interaction after 30 min of degradation (Figure 9h). These results highlight the interesting dynamics of the interaction between photocatalytic materials and the DP from treated water with cellular systems. The observed toxicity could arise from (1) the different mechanisms of interaction, (2) possible transformation of the tested samples, (3) oxidation of cell components such as lipids and proteins, or (4) the generation of reactive oxygen species.[85] Further studies are ongoing to assess the toxicity mechanism and the implications of the photocatalysts and the OTC degradation byproducts on water quality.

3. Conclusion

In summary, the novel MBOdCN S-scheme heterostructure with strong interfacial contact was successfully prepared by a simple in situ calcination method and utilized in visible light photocatalytic water remediation of OTC. The efficient S-scheme heterojunction mechanism of charge transfer in MBOdCN heterostructure was profoundly confirmed by XPS, DFT calculations, and work function measurements, respectively. The promotion of the photocatalytic performance of MBOdCN was closely investigated experimentally via trapping experiments and ESR analysis. The uplifted effect of charge transfer rates and the strong redox power of the MBOdCN S-scheme heterojunction are some of the important parameters to initiate photocatalytic reactions with improved activity. The presence of a dual charge transfer mechanism promoted by Bi-N linkages and Mg defects played a vital role in the photocatalytic performance via accelerating the reaction rate. Benefiting from the synergisms of n-π^* transition for enhanced light utilization and other mentioned parameters, the OTC degradation efficiency (99.56%) of the MBOdCN S-scheme heterojunction was 3.14 and 1.40 times higher than of pristine dCN and MBO, respectively. The nonselective pH heterojunction photocatalyst displayed high stability after five reuse cycles with an efficiency greater than 96.00%. The degradation pathways were studied with HPLC-TOF-MS/MS while toxicity was evaluated on human cells. This work highlights new horizons for the construction of novel S-scheme heterojunction photocatalytic with chemical bond bridges to fasten charge migration and isolation. This strategy can also be studied using other synthesis methods such as hydrothermal and evaluated on real wastewater remediation.

4. Experimental Section

Reagents and Chemicals: The chemical reagents purchased from Sigma–Aldrich (Merck), South Africa, were of analytical reagent grade and were used without further purification. Magnesium nitrate hexahydrate ($Mg(NO_3)_2{\cdot}6H_2O$, 99%), bismuth(III) nitrate pentahydrate ($Bi(NO_3)_3{\cdot}5H_2O$, ≥98.0%), isopropanol (C_3H_8O, ≥99.5%), sodium hydroxide (NaOH, ≥98%), tannic acid ($C_{76}H_{52}O_{46}$), cyanuric acid ($C_3H_3N_3O_3$, 98%), cetyltrimethylammonium bromide (CTAB, $C_{19}H_{42}BrN$, ≥98%), melamine ($C_3H_6N_6$, 99%), OTC ($C_{22}H_{24}N_2O_9$), hydrochloric acid (HCl, 37%), ethylenediaminetetraacetic acid (EDTA,

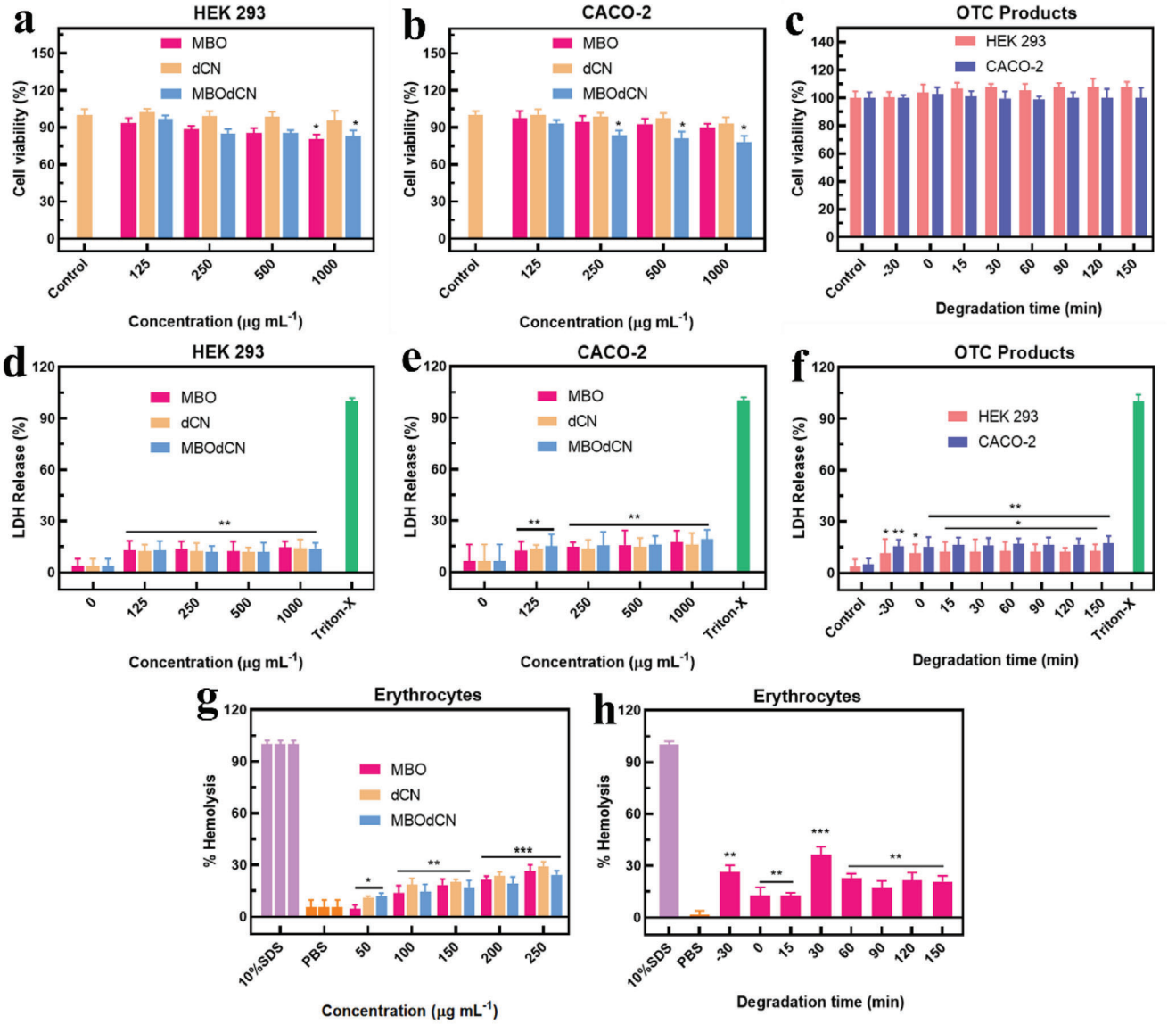

Figure 9. Investigation of the toxicity response of HEK293 and Caco-2 cells after exposure to photocatalysts (MBO, dCN, and MBOdCN and degradation products (oxytetracycline, OTC): a–c) cell viability and d–f) lactate dehydrogenase (LDH) assay at 24 h after treatment and g–h) hemolysis assay. One-way analysis of variance (ANOVA) and Wilcoxon signed-rank test were used to compare the differences between groups. The data are presented as the mean ± standard deviation ($n = 3$) with $^{*}p < 0.05$, $^{**}p < 0.01$, and $^{***}p < 0.001$.

$C_{10}H_{16}N_2O_8$, 99.4-100.6%), *p*-benzoquinone ($C_6H_4O_2$, ≥98%), sodium sulfate (Na_2SO_4, ≥99%), potassium hexacyanoferrate(III) ($K_3Fe(CN)_6$, ≥99.0%), potassium hexacyanoferrate(II) trihydrate ($K_4Fe(CN)_6{\cdot}3H_2O$, 98.5-102.0%), potassium chloride (KCl, 99.0-100.5%), acetone (C_3H_6O, ≥99.9%), polyvinylidene fluoride ($(-(C_2H_2F_2)_n-$, PVDF), and N-methyl-2-pyrrolidone (C_5H_9NO, NMP) were utilized. Ultrapure water obtained from a Millipore Milli–Q apparatus provided by Merck was used to prepare the solutions.

Photocatalyst Synthesis: The magnesium-bismuth oxide catalyst was produced using facile hydrothermal and calcination methods. First, 0.015 mol of $Mg(NO_3)_2{\cdot}6H_2O$ and 0.030 mol of $Bi(NO_3)_3{\cdot}5H_2O$ were sequentially added to a 150 mL mixture of deionized water and isopropanol (6.5:1 v/v) with stirring. Second, 0.150 mol of NaOH was added to the contents followed by 1 h agitation. The reaction solution was subsequently poured into the hydrothermal reactor and kept at 180 °C for 6 h. Upon cooling, the solid material was collected and washed by centrifugation before drying at 70 °C in an electric oven. The fine powder obtained was treated for 4 h at 550 °C in a muffle furnace using a 5 °C min^{-1} ramping rate. The resultant material (Mg-Bi_2O_3) was abbreviated as MBO.

The low bandgap graphitic carbon nitride was prepared by dissolution of a 1:10 mol ratio of tannic and cyanuric acids in 120 mL deionized water in a beaker. This was followed by the sequential addition of a 1:3 w/w ratio of CTAB to melamine. Immediately after, the solution turned from a faint yellow to a creamy whitish emulsion. The mixture was stirred for 1 h at 700 rpm and 90 °C. Thereafter, the contents were poured into a Teflon-lined autoclave reactor and kept at 180 °C for 24 h prior to drying at 100 °C in the oven. The dark gray powder was annealed at 550 °C for 4 h in a muffle furnace at a ramp rate of 5 °C min^{-1} to obtain ash-like dark gray graphitic carbon nitride, abbreviated as dCN.

The composite materials (MBOdCN) were prepared from precursors of MBO and dCN before they were annealed. Generally, a mass ratio of 3:1, 1:1, 1:3, and 1:5 MBO:dCN was used. The contents were mixed thoroughly

using a mortar and pestle for approximately 30 min before being placed in lidded crucibles for heating under the same conditions as those used for the pristine materials. The yellow- and orange-colored catalysts were collected and stored for subsequent experiments.

Photocatalytic Performance: The OTC (10 mg L^{-1}) was used as a model pollutant to evaluate the photocatalytic power of the MBOdCN heterojunction under visible light irradiation. The 300 W Xe lamp with a cutoff filter of 420 nm (HAL-320 solar simulator, ASAHI SPECTRA, Japan) was used as a source of visible light. Initially, 20 mg of catalyst was evenly distributed by stirring in 50 mL of OTC (10 mg L^{-1}) in the dark for 30 min to achieve adsorption saturation. In the process of photocatalysis, about 4 mL aliquots were sampled at a specified period and passed through CHMLAB PES 0.45 µm syringe filters before studying the degradation with a PerkinElmer Lambda 650S UV–Vis spectrophotometer. The degradation process was performed in triplicate for statistical purposes. The removal efficiency (η) and pseudo-first-order kinetics were conducted as follows: $\eta = (C_0 - C_t/C_0) \times 100$ and $ln(C_0/C_t) = k_{app}t$, where C_0, C_t, and k_{app} refer to the initial concentration, the final concentration of the OTC solution at the specified time, and the apparent rate constant of the degradation process, respectively.

The contributions of various reactive species radicals were evaluated using quenching chemicals such as isopropanol, *p*-benzoquinone, and EDTA as quenchers for hydroxyl radicals ($^{\bullet}OH$), superoxide radicals ($^{\bullet}O_2^-$), and holes (h^+), respectively. To further identify the reactive species produced during OTC degradation, ESR signals of $^{\bullet}O_2^-$ and $^{\bullet}OH$ spin-trapped radicals were measured in the dark and under visible light on a JEOL JES-FA200 ESR spectrometer employing 5,5-dimethyl-1-pyrroline-*N*-oxide (DMPO) as a spin-capture reagent. Moreover, a recyclability study was performed to determine the stability of the photocatalyst. After each cycle, the photocatalyst was recovered from the reaction mixture via centrifugation, washed, dried, and reintroduced to a fresh OTC solution. This process was repeated five times. Since slurry photocatalysis is prone to catalyst loss, parallel reactions were set up under the same conditions to obtain enough catalyst for recyclability studies.

Characterization Techniques and Photoelectrochemical Assessment: Specific information on characterization techniques and photoelectrochemical analysis is given in detail under Text S1 and S2 (Supporting Information).

Analytical Techniques: The techniques include the fluorescence excitation-emission matrices (EEMS) were recorded using HORIBA Aqualog Yobin Yvon spectrometer and high-performance liquid chromatography time-of-flight-tandem mass spectrometry (HPLC-TOF-MS/MS). They were performed as illustrated in our previous work.[18]

Density Functional Theory (DFT) Calculations: All calculations and simulations were performed using the Quantum Espresso package code.[86] The optimized norm-conserving Vanderbilt pseudopotentials were used to explain the interaction between ions and electrons, and the exchange-correlation energy of the electron–electron interactions was considered using the Perdew–Burke–Ernzerhof generalization of the generalized gradient approximation.[87] Bi ($6s^2\ 6p^3$), O ($2s^2\ 2p^4$), Mg ($3s^2$), C ($2s^2\ 2p^2$), and N ($2s^2\ 2p^3$) were treated as valence electrons. To obtain more reliable electronic properties, the Heyd–Scuseria–Enzerhof (HSE06) hybrid functional, which uses the screened exchange Hartree–Fock approach, was employed. The Grimme DFTD3(BJ) approach was used to treat long-range van der Waal (vdW) interactions, and a vacuum gap of 25 Å along the *Z*-axis was chosen to prevent interactions between adjacent layers.[88] In addition, dipole correction was used to remove electrostatic potential errors emanating from periodic boundary conditions. With the conjugate gradient algorithm of the Broyden–Fletcher–Goldfarb–Shanno method, the kinetic cutoff and charge density energy were set to 35 and 360 Ry, respectively, while 10^{-6} eV and 0.001 eV $Å^{-1}$ were set as the total energy convergence criterion and residual forces, respectively, after the convergence tests. The Monkhorst-pack was utilized with $9 \times 9 \times 1$ k-point for all the calculations. The phonon dispersion graphs were obtained using density functional perturbation theory within the phonon code. The thermal stability was investigated via ab initio molecular dynamics (AIMD) calculations for 25 ps at 300 K with a time step of 1 fs and the Nosé–Hoover scheme. The structures were visualized using VESTA software.

Cell Cytotoxicity Studies: The photocatalysts and OTC degradation byproducts were exposed to relevant cell lines and red blood cells to ascertain their safety. Briefly, human intestinal epithelial (CACO-2) and human embryonic kidney (HEK293) cells cultured in Dulbecco's modified Eagle's medium (DMEM; Merck South Africa) supplemented with 10% fetal bovine serum (FBS) and 1% penicillin-streptomycin at 37 °C and 5% CO_2 were seeded at 2×10^5 cells mL^{-1} in 96-well culture plates (TPP, Switzerland). After 24 h incubation, both cells were treated with the photocatalysts at a concentration range of 125–1000 µg mL^{-1} and further incubated for 24 h. Also, the degradation products obtained at each degradation time point were exposed to both cells at the same concentration range as those of the photocatalysts under the same condition. Thereafter, the toxicity of the samples was measured using either the metabolic activity assay kit (CellTitre-Blue, Promega, Madison, WI, USA) or the membrane integrity using an LDH assay kit (CytoTox-ONE; Promega) according to the manufacturer's instructions. For the hemolysis assay, blood samples were collected inside an EDTA tube, and the erythrocytes were centrifuged at 1600 rpm for 10 min at 20 °C. The cells were washed with PBS three times and resuspended in phosphate buffer saline (PBS) supplemented with 10% (v/v) red blood cells. Thereafter, a 1:10 dilution was made using PBS, and 100 µL of this suspension was treated with the photocatalysts (50–250 µg mL^{-1}) and degradation byproducts for 1 h at 37 °C. SDS (10%) and PBS were used as the positive and negative controls, respectively.

Supporting Information

Supporting Information is available from the Wiley Online Library or from the author.

Acknowledgements

This work was financially supported by the National Research Foundation (NRF) (Grant number: PSTD22051410627) of South Africa and the University of South Africa (UNISA). The authors are grateful to the Department of Physics (UNISA) for providing technical support toward accomplishing the work. The Department of Life and Consumer Sciences (UNISA) is acknowledged for assisting with toxicity studies. The computational support and resources from the Center for High-Performance Computing (CHPC), Cape Town, South Africa, are also acknowledged.

Conflict of Interest

The authors declare no conflict of interest.

Author Contributions

P.J.M. worked on conceptualization, methodology, investigation, data curation, formal analysis, wrote original draft, and reviewed and edited the work. M.E.M.: investigated the work, performed methodology, and reviewed and edited the work. F.O. performed formal analysis, helped in software, and wrote the original draft. A.O.O. performed the investigation, reviewed and edited the writing. G.M. wrote the original draft, reviewed and edited the writing. T.L.Y. performed methodology, and investigation. J.F.N. reviewed and edited the writing. S.L.L. reviewed and edited the writing. D.L. performed validation, reviewed and edited the writing. J.G. performed validation, reviewed and edited the writing. B.B.M. performed the conceptualization, validation, and resources. A.T.K. performed the conceptualization, validation, reviewed and edited the writing, and also funding acquisition. All the authors have approved the final version of the manuscript.

Data Availability Statement

The data used in the work will be made available upon reasonable request.

Keywords

ecotoxicity, linked interface, oxytetracycline, photocatalysis, S-scheme

Received: December 30, 2024
Revised: February 10, 2025
Published online: February 26, 2025

[1] A. J. Browne, M. G. Chipeta, G. Haines-Woodhouse, E. P. A. Kumaran, B. H. K. Hamadani, S. Zaraa, N. J. Henry, A. Deshpande, R. C. Reiner, N. P. J. Day, A. D. Lopez, S. Dunachie, C. E. Moore, A. Stergachis, S. I. Hay, C. Dolecek, *Lancet Planet Health* **2021**, *5*, e893.
[2] T. Senasu, N. Lorwanishpaisarn, K. Hemavibool, S. Nijpanich, N. Chanlek, S. Nanan, *Sep. Purif. Technol.* **2023**, *306*, 122735.
[3] Z. Zhang, H. He, T. Han, X. Tian, J. Pang, H. Lambers, *Appl. Soil Ecol.* **2023**, *187*, 104861.
[4] P. J. Mafa, M. E. Malefane, F. Opoku, J. Gui, D. Liu, B. B. Mamba, A. T. Kuvarega, *J. Water Process Eng.* **2024**, *68*, 106405.
[5] H. Sun, T. Zhou, J. Kang, Y. Zhao, Y. Zhang, T. Wang, X. Yin, *Sep. Purif. Technol.* **2022**, *299*, 121771.
[6] M. E. Malefane, P. J. Mafa, M. Managa, T. T. I. Nkambule, A. T. Kuvarega, *Adv. Sustainable Syst.* **2025**, *9*, 2400434.
[7] H. Zhu, Z. Guo, W. Yu, S. Yuan, L. Shen, D. L. Zhao, H. Lin, *Water Res.* **2025**, *272*, 122919.
[8] H. Wang, Y. Cao, B. Li, L. Shen, X. L. Wu, R. Li, H. Lin, *Water Res.* **2025**, *268*, 122623.
[9] N. Mukwevho, P. J. Mafa, K. K. Kefeni, A. K. Mishra, S. B. Mishra, A. T. Kuvarega, *J. Water Process Eng.* **2024**, *65*, 105882.
[10] R. Selvaraj, K. R. Kalimuthu, V. Kalimuthu, *Mater. Lett.* **2019**, *243*, 183.
[11] A. Mehtab, S. Banerjee, Y. Mao, T. Ahmad, *ACS Appl. Mater. Interfaces* **2022**, *14*, 44317.
[12] X. Ren, X. Zhang, R. Guo, X. Li, Y. Peng, X. Zhao, *Sep. Purif. Technol.* **2021**, *270*, 118797.
[13] M. E. Malefane, P. J. Mafa, M. Managa, T. T. I. Nkambule, A. T. Kuvarega, *Phys. Chem. Lett.* **2023**, *14*, 1029.
[14] L. Wang, J. Sun, B. Cheng, R. He, J. Yu, *J. Phys. Chem. Lett.* **2023**, *14*, 4803.
[15] Q. Xu, L. Zhang, B. Cheng, J. Fan, J. Yu, *Chem* **2020**, *6*, 1543.
[16] H. Ge, F. Xu, B. Cheng, J. Yu, W. Ho, *ChemCatChem* **2019**, *11*, 6301.
[17] J. Fu, Q. Xu, J. Low, C. Jiang, J. Yu, *Appl. Catal., B* **2019**, *243*, 556.
[18] P. J. Mafa, M. E. Malefane, F. Opoku, A. Sacko, A. O. Oladipo, S. L. Lebelo, D. Liu, J. Gui, B. B. Mamba, A. T. Kuvarega, *J. Cleaner Prod.* **2023**, *429*, 139519.
[19] M. E. Malefane, P. J. Mafa, P. P. Mamba, M. Managa, T. T. I. Nkambule, A. T. Kuvarega, *Chem. Eng. J.* **2024**, *480*, 148250.
[20] X. Jia, J. Cao, H. Sun, X. Li, H. Lin, S. Chen, *Appl. Catal., B* **2024**, *343*, 123522.
[21] X. Zhang, Y. Song, X. Niu, X. Lin, S. Zhong, H. Lin, B. Teng, S. Bai, *Appl. Catal., B* **2024**, *342*, 123445.
[22] K. K. Bera, R. Majumdar, M. Chakraborty, S. K. Bhattacharya, *J. Hazard. Mater.* **2018**, *352*, 182.
[23] M. Weber, R. D. Rodriguez, D. R. T. Zahn, K. Stöwe, M. Mehring, *Inorg. Chem.* **2022**, *61*, 1571.
[24] Y. Wang, S. Xue, Y. Liao, H. Wang, Q. Lu, N. Tang, F. Du, *J. Environ. Manage.* **2024**, *362*, 121342.
[25] H. Han, S. Zhang, S. Song, W. Zhang, D. Liu, Z. Song, Q. Wang, C. Ma, S. Feng, X. Duan, *Appl. Surf. Sci.* **2024**, *662*, 160122.
[26] C. Kong, Y. Liu, H. Zeng, L. Zhang, W. Wang, J. Li, H. Wu, K. Wu, J. Guo, *J. Environ. Chem. Eng.* **2023**, *11*, 111551.
[27] L. Zhang, Y. Meng, H. Shen, J. Li, C. Yang, B. Xie, S. Xia, *Appl. Surf. Sci.* **2021**, *567*, 150760.
[28] D. Majhi, A. Kumar Mishra, K. Das, R. Bariki, B. G. Mishra, *Chem. Eng. J.* **2021**, *413*, 127506.
[29] W. Zhang, Q. Tan, T. Liu, Y. He, G. Chen, K. Chen, D. Han, D. Qin, L. Niu, *Mater. Horiz.* **2023**, *10*, 5869.
[30] H. Liu, F. Sun, X. Li, Q. Ma, G. Liu, H. Yu, W. Yu, X. Dong, Z. Su, *Composites, Part B* **2023**, *259*, 110746.
[31] P. Zhou, Y. Wang, X. Yan, Y. Gan, C. Xia, Y. Xu, M. Xie, *Appl. Catal., B* **2024**, *343*, 123485.
[32] Z. Zhao, Z. Wang, J. Zhang, C. Shao, K. Dai, K. Fan, C. Liang, *Adv. Funct. Mater.* **2023**, 33, 2214470.
[33] X. Zhang, D. Kim, J. Yan, L. Y. S. Lee, *ACS Appl. Mater. Interfaces* **2021**, *13*, 9762.
[34] M. Gao, Z. Li, X. Su, X. Zhang, J. Chang, D. Geng, Y. Lu, H. Zhang, T. Wei, J. Feng, *Chemosphere* **2023**, *343*, 140285.
[35] T. Li, X. Wang, Z. Jin, N. Tsubaki, *Chem. Eng. J.* **2023**, *477*, 147018.
[36] Y. Zhang, J. Di, X. Zhu, M. Ji, C. Chen, Y. Liu, L. Li, T. Wei, H. Li, J. Xia, *Appl. Catal., B* **2023**, *323*, 122148.
[37] Z. He, C. Qian, D. Chen, K. Xu, W. Hao, *J. Colloid Interface Sci.* **2023**, *651*, 138.
[38] J. Ma, L. Xu, Z. Yin, Z. Li, X. Dong, Z. Song, D. Chen, R. Hu, Q. Wang, J. Han, Z. Yang, J. Qiu, Y. Li, *Appl. Catal., B* **2024**, *344*, 123601.
[39] L. Li, H. Feng, Z. Dong, T. Yang, S. Xue, *J. Colloid Interface Sci.* **2023**, *649*, 10.
[40] Z. Jin, T. Li, K. Wang, X. Guo, *J. Colloid Interface Sci.* **2022**, *609*, 212.
[41] Q. Liu, Z. Yu, D. Liang, J. Xiong, T. Gan, H. Hu, Z. Huang, Y. Zhang, *Chem. Eng. J.* **2024**, *496*, 154057.
[42] X. Huang, R. Du, Y. Zhang, J. Ren, Q. Yang, K. Wang, Y. Ni, Y. Yao, R. Ali Soomro, L. Guo, C. Yang, D. Wang, B. Xu, F. Fu, *J. Colloid Interface Sci.* **2024**, *664*, 33.
[43] S. Li, L. Meng, W. Tian, L. Li, *Adv. Energy Mater.* **2022**, *12*, 2200629.
[44] K. Wang, L. Peng, X. Shao, Q. Cheng, J. Wang, K. Li, H. Wang, *Sol. RRL* **2022**, *6*, 2200434.
[45] P. Hao, Z. Chen, Y. Yan, W. Shi, F. Guo, *Sep. Purif. Technol.* **2024**, *330*, 125302.
[46] B. Zhang, Y. Liu, D. Wang, W. He, X. Fang, C. Zhao, J. Pan, D. Liu, S. Liu, T. Chen, L. Zhao, J. Wang, *Sep. Purif. Technol.* **2025**, *354*, 128893.
[47] S. Zhang, J. Chen, C. Fang, Y. Zhang, Z. Xu, Z. Yan, K. Yao, *Colloids Surf., A* **2023**, *664*, 131165.
[48] P. J. Mafa, M. E. Malefane, A. O. Idris, D. Liu, J. Gui, B. B. Mamba, A. T. Kuvarega, *Sep. Purif. Technol.* **2022**, *282*, 120089.
[49] B. Y. Balarabe, S. Paria, D. Sekou Keita, A. Razak Ibrahim Baraze, E. Kalugendo, G. Nii Tetteh Tetteh, M. Merycleopha Meringo, M. Nasser Illiassou Oumarou, *Inorg. Chem. Commun.* **2022**, *146*, 110204.
[50] B. Karthikeyan, R. Udayabhaskar, A. Kishore, *Appl. Phys. A: Mater. Sci. Process.* **2014**, *117*, 1409.
[51] K. M. Alam, N. Chaulagain, E. Shahini, M. Masud Rana, J. Garcia, N. Kumar, A. E. Kobryn, S. Gusarov, T. Tang, K. Shankar, *Chem. Eng. J.* **2023**, *456*, 141067.
[52] M. J. Madito, *ACS Appl. Mater. Interfaces* **2021**, *13*, 37014.
[53] S. Panimalar, R. Uthrakumar, E. T. Selvi, P. Gomathy, C. Inmozhi, K. Kaviyarasu, J. Kennedy, *Surf. Interfaces* **2020**, *20*, 100512.
[54] P. J. Mafa, A. T. Kuvarega, B. B. Mamba, B. Ntsendwana, *Appl. Surf. Sci.* **2019**, *483*, 506.
[55] J. Yue, H. Yang, S. Wang, C. Liu, L. Wang, *J. Colloid Interface Sci.* **2024**, *653*, 981.
[56] Y. J. Hao, B. Liu, L. G. Tian, F. T. Li, J. Ren, S. J. Liu, Y. Liu, J. Zhao, X. J. Wang, *ACS Appl. Mater. Interfaces* **2017**, *9*, 12687.
[57] X. Wang, Z. Li, Y. Zhang, Q. Li, H. Du, F. Liu, X. Zhang, H. Mu, J. Duan, *Chem. Eng. J.* **2022**, *429*, 132270.
[58] S. Singh, R. K. Sahoo, N. M. Shinde, J. M. Yun, R. S. Mane, W. Chung, K. H. Kim, *RSC Adv.* **2019**, *9*, 32154.
[59] J. Shao, H. Fei, H. Li, L. Yang, M. Li, J. Gao, H. Liao, J. Lu, *Sep. Purif. Technol.* **2022**, *297*, 121515.
[60] Z. Liu, C. Li, Y. Xu, Y. Jiao, Y. Liu, L. Wang, *Opt. Mater.* **2023**, *139*, 113773.
[61] P. J. Mafa, M. E. Malefane, F. Opoku, B. B. Mamba, A. T. Kuvarega, *Chem. Eng. J.* **2023**, *464*, 142462.

[62] S. Zwane, T. Ingwani, D. S. Dlamini, B. B. Mamba, A. T. Kuvarega, *J. Photochem. Photobiol., A* **2024**, *446*, 115123.
[63] X. Zhang, C. Li, J. Liang, S. Yang, F. Yuan, S. Zheng, J. Yi, Z. Sun, *J. Membr. Sci.* **2023**, *685*, 121924.
[64] H. Huang, T. T. Xu, B. L. Wang, N. Lv, Y. T. Zhang, *Sep. Purif. Technol.* **2023**, *307*, 122848.
[65] W. Zhao, M. Yan, X. Yang, X. Zeng, Y. Chen, B. Dai, X. Chu, X. Hong, F. Mu, S. Li, D. Y. C. Leung, *Sep. Purif. Technol.* **2023**, *308*, 122896.
[66] C. Zhao, M. Pelaez, X. Duan, H. Deng, K. O'Shea, D. Fatta-Kassinos, D. D. Dionysiou, *Appl. Catal., B* **2013**, *134–135*, 83.
[67] J. Shi, M. Tai, J. Hou, Y. Qiao, C. Liu, T. Zhou, L. Wang, B. Hu, *Chem. Eng. J.* **2023**, *456*, 141029.
[68] F. Wang, T. He, Y. Gao, Y. Li, S. Cui, H. Huang, J. Yang, *Sep. Purif. Technol.* **2023**, *325*, 124596.
[69] Y. Chen, S. Dong, H. Zhang, Y. Wei, B. Wang, Y. Zhang, *Sep. Purif. Technol.* **2023**, *318*, 124024.
[70] T. J. Al-Musawi, P. Rajiv, N. Mengelizadeh, F. Sadat Arghavan, D. Balarak, *J. Mol. Liq.* **2021**, *337*, 116470.
[71] Y. Liu, T. Hu, S. He, L. Feng, Q. Zhao, J. Jiang, L. Wei, *Chem. Eng. J.* **2023**, *477*, 146867.
[72] Y. Wu, X. Zhao, Y. Li, Y. Ling, Y. Zhang, X. Zhang, S. Huang, *Chemosphere* **2022**, *302*, 134862.
[73] W. Xu, Q. Zhang, K. Xu, L. Qiu, J. Song, L. Wang, *Chemosphere* **2022**, *307*, 135811.
[74] L. Shi, J. Yin, Y. Liu, H. Liu, H. Zhang, H. Tang, *Chemosphere* **2022**, *309*, 136607.
[75] J. Ding, C. Li, H. Yin, Y. Zhou, S. Wang, K. Liu, M. Li, J. Wang, *Environ. Pollut.* **2023**, *327*, 121550.
[76] S. Zhang, S. Zhao, S. Huang, B. Hu, M. Wang, Z. Zhang, L. He, M. Du, *Chem. Eng. J.* **2021**, *420*, 130516.
[77] S. Wang, H. Yin, J. Ding, H. Chen, L. Wang, Y. Zhou, K. Liu, J. Wang, *Surf. Interfaces* **2023**, *37*, 102642.
[78] C. Feng, Z. Lu, Y. Zhang, Q. Liang, M. Zhou, X. Li, C. Yao, Z. Li, S. Xu, *Chem. Eng. J.* **2022**, *435*, 134833.
[79] M. E. Malefane, P. J. Mafa, T. T. I. Nkambule, M. E. Managa, A. T. Kuvarega, *Chem. Eng. J.* **2023**, *452*, 138894.
[80] T. S. Ntelane, U. Feleni, N. H. Mthombeni, A. T. Kuvarega, *Colloids Surf., A* **2022**, *655*, 130276.
[81] X. Tan, W. Cen, G. Qian, Q. Chen, Q. Xie, *Mater. Sci. Semicond. Process.* **2023**, *167*, 107779.
[82] T. L. Yusuf, S. A. Ogundare, F. Opoku, O. A. Arotiba, N. Mabuba, *J. Environ. Chem. Eng.* **2023**, *11*, 110711.
[83] X. Dong, L. Xu, J. Ma, Y. Li, Z. Yin, D. Chen, Q. Wang, J. Han, J. Qiu, Z. Yang, Z. Song, *Chem. Eng. J.* **2023**, *459*, 141557.
[84] S. Bose, M. Maruthupandy, W. S. Cho, H. W. Kang, *Surf. Interfaces* **2023**, *39*, 102891.
[85] C. M. Vineeth Kumar, V. Karthick, V. G. Kumar, D. Inbakandan, E. R. Rene, K. S. U. Suganya, A. Embrandiri, T. S. Dhas, M. Ravi, P. Sowmiya, *Environ. Res.* **2022**, *212*, 113202.
[86] P. Giannozzi, S. Baroni, N. Bonini, M. Calandra, R. Car, C. Cavazzoni, D. Ceresoli, G. L. Chiarotti, M. Cococcioni, I. Dabo, A. Dal Corso, S. De Gironcoli, S. Fabris, G. Fratesi, R. Gebauer, U. Gerstmann, C. Gougoussis, A. Kokalj, M. Lazzeri, L. Martin-Samos, N. Marzari, F. Mauri, R. Mazzarello, S. Paolini, A. Pasquarello, L. Paulatto, C. Sbraccia, S. Scandolo, G. Sclauzero, A. P. Seitsonen, et al., *J. Phys.: Condens. Matter* **2009**, *21*, 395502.
[87] J. P. Perdew, K. Burke, M. Ernzerhof, *Phys. Rev. Lett.* **1996**, *77*, 3865.
[88] S. Grimme, S. Ehrlich, L. Goerigk, *J. Comput. Chem.* **2011**, *32*, 1456.